

CO OUTFLOWS FROM YOUNG STARS: CONFRONTING THE JET AND WIND MODELS

CHIN-FEI LEE AND LEE G. MUNDY

Astronomy Department, University of Maryland, College Park, MD 20742; chinfei@astro.umd.edu, lgm@astro.umd.edu

BO REIPURTH

Center for Astrophysics and Space Astronomy, University of Colorado, Boulder, CO 80309; reipurth@casa.Colorado.edu

AND

EVE C. OSTRIKER AND JAMES M. STONE

Astronomy Department, University of Maryland, College Park, MD 20742; ostriker@astro.umd.edu, jstone@astro.umd.edu

Received 2000 April 3; accepted 2000 May 5

ABSTRACT

We have mapped the CO $J = 1-0$ emission from molecular outflows associated with five young stellar systems of class 0 to class II/III using the BIMA array and the FCRAO 14 m antenna. The systems, VLA 05487, HH 212, HH 240/241, HH 111, and RNO 91, are all relatively nearby and of low luminosity, and the majority have H₂ emission or optical jet features. The CO outflow generally forms a shell structure around the outflow axis with the higher velocity emission further out from the source. Two distinctive kinematic features are evident in position-velocity (PV) diagrams: a parabolic structure originating at the driving source (e.g., VLA 05487 and HH 111) and a convex spur structure with the high-velocity tip near known H₂ bow shocks (e.g., HH 212, HH 240/241 and HH 111). The parabolic PV structure can be produced by a wide-angle-wind model, while the velocity spur structure can be modeled with a jet-driven bow shock model. VLA 05487, which is not associated with any H₂ bow shocks, shows only the parabolic structure and kinematics consistent with the wide-angle wind-driven model. HH 212, which is associated with a series of H₂ bow shock structures, shows a striking morphological coincidence between the H₂ and CO emission and velocity spurs in the PV diagram. It is our best example of the jet-driven bow shock model, and its kinematics can be qualitatively explained in that context. HH 240/241 is similar to HH 212 and shows a close relationship between the H₂ and CO emission. The kinematics of its western lobe can also be explained with the jet-driven model. The kinematics of RNO 91 are similar to VLA 05487 and are broadly consistent with a wide-angle wind-driven model. HH 111 has both parabolic and spur PV structures, a combination that is not easily explained in the simplest version of either model.

Thus, these observations provide examples of systems that support either the wide-angle wind-driven or jet-driven model in the simplest interpretation. More detailed calculations are needed to understand whether one model might be able to fit all systems. It is crucial to know if time-dependent or long-lived jet-driven bow shock models can produce the observed outflow widths and parabolic PV structures, or if a wide-angle wind can produce the shock features and velocity spur structures in our observations.

Subject headings: ISM: individual (VLA 05487, HH 212, HH 240/241, HH 111, RNO 91) —

ISM: jets and outflows — stars: formation

1. INTRODUCTION

Molecular outflows are associated with stars in the early stages of stellar evolution (Bally & Lada 1983; Lada 1985; Fukui et al. 1993; Wu, Huang, & He 1996). The observational properties of molecular outflows are summarized in Masson & Chernin (1993), Bachiller (1996), Cabrit, Raga, & Gueth (1997), and Richer et al. (2000). In brief, a molecular outflow consists of low-velocity molecular material which traces the interaction between the ambient cloud and high-velocity material emanating from young and forming stars. The outflows are generally bipolar in morphology and best imaged in CO and other common simple molecules. In many sources, the velocities in the molecular outflows increase with distance from the source. At low velocities, the outflow appears as a limb-brightened shell surrounding a cavity, while at high velocities the outflow sometimes becomes more jetlike. In typical outflows, there is little overlap of blueshifted and redshifted emission within the individual lobes, suggesting that the molecular outflow has small transverse motions compared to motions along

the outflow axis (Meyers-Rice & Lada 1991; Lada & Fich 1996).

A number of models have been proposed to explain the morphology and kinematics of molecular outflows. Currently, the jet-driven bow shock model (Raga & Cabrit 1993; Masson & Chernin 1993; Chernin et al. 1994) and the wind-driven-shell model (Shu et al. 1991; Li & Shu 1996; Shu et al. 2000) are the standards of the field. In the jet-driven bow shock model, a jet propagates into the ambient material and forms a bow shock surface at the head of the jet. As the bow shock moves away from the star, it interacts with the ambient material and produces the molecular outflow around the jet. A number of simulations have been carried out to investigate this mechanism (Stone & Norman 1994; Suttner et al. 1997; Smith, Suttner, & Yorke 1997; Völker et al. 1999). In the wind-driven-shell model, the young star expels a wide-angle magnetized wind that snowplows into the ambient material. The ambient material is radially swept up by a forward shock that runs ahead of the wind bubble and produces the molecular outflow (Shu et al.

2000; Matzner & McKee 1999). If the wind has an axial density gradient, the core of the wind can take on the appearance of a collimated jet (Shu et al. 1995; Ostriker 1997; Shang, Shu, & Glassgold 1998).

These two models have been used to explain the morphology and energetics of a number of molecular outflows, e.g., HH 211 (jet-driven model; Gueth & Guilloteau 1999) and HH 111 (wind-driven model; Nagar et al. 1997). However, neither model can entirely explain the broad range in observed outflow morphologies. In particular, the jet-driven bow shock model produces outflow lobes that are too narrow and have excessive transverse velocities, whereas the wind-driven-shell model has difficulties producing highly collimated outflows and the observed shock-heated molecular features at the cavity ends (Cabrit et al. 1997). The recent detection of multiple cavities in some CO molecular outflows (in e.g., L1157 in Gueth, Guilloteau, & Bachiller 1996) presents further challenges for any steady state flow models.

In this paper, we present detailed CO $J = 1-0$ maps of five outflow systems with different collimations and sources in different evolutionary stages. The systems are VLA 05487+0255 (hereafter VLA 05487), HH 212, HH 111, HH 240/241, and RNO 91. The driving sources are class 0/I sources for VLA 05487, HH 212, and HH 240/241, a class I source for HH 111, and a class II/III source for RNO 91, allowing us some insight into molecular outflows at different evolutionary stages. Except for RNO 91, the molecular outflows are known to be associated with jetlike or bow shock structures in H_2 , allowing us to investigate the direct connection between the molecular outflows and protostellar jets. In § 2 we summarize our observing and data reduction procedures for the BIMA and FCRAO CO observations. In § 3 we present, for each outflow system, the integrated and channel maps, the comparison of the flux profiles between the BIMA and FCRAO observations, and the position-velocity diagrams cut along the outflow axis. In § 4 we discuss our observations and confront the various features seen in our observations with those predicted in the jet-driven and wide-angle wind-driven models. The shell structure and position-velocity diagrams for these theoretical models are presented in §§ 4.1.1 and 4.1.2; readers may wish to consult this section to preview the characteristic features of each model prior to examining the data of § 3. We conclude in § 5 with a summary of our observational results and their relation to the predictions of jet and wind

models. More detailed numerical simulations of jet-driven and wind-driven outflow models will appear in a forthcoming publication.

2. OBSERVATIONS AND DATA REDUCTION

Observations of the CO $J = 1-0$ line toward the VLA 05487, HH 111, HH 212, HH 240/241, and RNO 91 regions were obtained with the BIMA 10-antenna interferometry array at Hat Creek California from 1996 to 1999, and with the FCRAO 14 m single dish at Amherst Massachusetts in 1999 April. The driving sources of the molecular outflows are listed with their positions in Table 1. For the BIMA observations, we used cross correlation mode 7 with 256 spectral channels in a bandwidth of 20 MHz. At an observing frequency of 115.271 GHz, this produces a velocity resolution of 0.27 km s^{-1} per channel and a total velocity coverage of 78 km s^{-1} . For FCRAO observations, we used the 16 element focal plane array receiver SEQUOIA with FAAS autocorrelation spectrometers. The spectrometers were set up with 512 channels in a bandwidth of 40 MHz, giving a similar velocity resolution to that of the BIMA interferometry data.

In the BIMA observations, the VLA 05487 region was first observed with three pointings in the C array: one pointing toward VLA 05487, one toward knot HH 110A, and one about $1'$ to the south of VLA 05487. VLA 05487 is found to be the source driving the prominent north-south oriented bipolar CO outflow detected at low angular resolution by Reipurth & Olberg (1991). Since the north lobe of the outflow is not contaminated by the outflow of IRS 1, which is to the south of VLA 05487, we further observed it with two pointings in the C and D arrays to study its structure. HH 212 was observed with four pointings aligned along the jet axis in the C and D arrays, with one pointing toward the driving source, one to the north and two to the south. The HH 240/241 outflow is $6'$ in extent; we observed it with five pointings in the C and D arrays, with the central pointing toward the driving source. HH 111 was observed with two pointings to the west of the driving source in the C and D arrays. Since it has small compact structure near the source, we further observed it in the B array. RNO 91 was observed with three pointings with one at the driving source and two to the south in the C and D arrays.

In each BIMA observation, a phase calibrator was observed every 10 to 15 minutes in B array, every 15 to 20

TABLE 1
MOLECULAR OUTFLOWS AND THE DRIVING SOURCES.

Outflow	Driving Source	α (2000)	δ (2000)	Class	Distance (pc)
VLA 05487	VLA 05487+0255	5 51 22.68 ^a	2 56 06.0	0/I	460
HH 212	IRAS 05413-0104	5 43 51.4 ^b	-1 02 52	0/I	460
HH 240/241	IRAS 05173-0555	5 19 48.86 ^c	-5 52 04.9	0/I	460
HH 111	HH 111 VLA	5 51 46.28 ^d	2 48 29.4	I	460
RNO 91	IRAS 16316-1540	16 34 29.3 ^e	-15 47 01	II/III	160

NOTE.—Units of right ascension are hours, minutes, and seconds, and units of declination are degrees, arcminutes, and arcseconds.

^a VLA position provided by Rodriguez et al. 1998.

^b 3.5 cm VLA position listed in Claussen et al. 1998.

^c 1.3 mm continuum position listed in Reipurth et al. 1993.

^d 3.6 cm VLA position listed in Rodriguez & Reipurth 1994.

^e IRAS position listed in Myers et al. 1988.

minutes in C array, and every 20 to 25 minutes in D array to calibrate the phases of the sources. A planet was also observed to calibrate the fluxes. The data were processed with the MIRIAD package. Since each observation contained more than one pointing, mosaicking techniques were used to convert the calibrated data into the dirty maps. The dirty maps were then deconvolved using the maximum entropy method with the Gull measure. The final channel maps were obtained by convolving the deconvolved dirty maps with a synthesized beam that best fitted the dirty beam. The channel maps have a synthesized beam size of about $4''$ and a noise level of $0.35 \text{ Jy beam}^{-1}$ for the B array observations, about $8''$ and $0.75 \text{ Jy beam}^{-1}$ for the C array observations, and about $15''$ and $1.75 \text{ Jy beam}^{-1}$ for the D array observations. B, C and D array observations were combined to obtain maps of intermediate angular resolution.

In the FCRAO observations, each outflow except for VLA 05487, was observed with full sampling, covering a $6'$ region around the driving sources, in position switching mode. VLA 05487 was not observed. The system temperatures were about 450 K, giving a noise level of 0.2 K. The data were processed with the CLASS package. Linear baselines were subtracted from the spectra and the maps were made with the GRID routine. The maps have an angular resolution of $46''$.

3. RESULTS

Figures 1–5 present CO maps from the BIMA observations for VLA 05487, HH 112, HH 240/241, HH 111, and

RNO 91, respectively. Figures 6–10 present position-velocity diagrams cut along the outflow axis for VLA 05487, HH 112, HH 240/241, HH 111, and RNO 91, respectively. We present these maps together to facilitate comparison of the outflow features. The following subsections describe the observational results for each of these outflow systems in detail.

3.1. VLA 05487

Located in the Orion dark cloud L 1617, VLA 05487 is at a distance of 460 pc. A bipolar CO $J = 1-0$ outflow, extending $10'$ to the north–south, was found in this region at low angular resolution and the *IRAS* data show an infrared source, IRAS 05487+0255, which was proposed to be the driving source (Reipurth & Olberg 1991). About $25''$ to the west of the formal position of *IRAS* source, there are two bright *K*-band sources, IRS 1 and IRS 2 (Davis, Mundt, & Eisloffel 1994); about $25''$ to the southeast is the HH 110 jet region. Near infrared images in H_2 emission toward the IRS sources revealed that IRS 2 is associated with a bipolar jet aligned with the CO outflow and IRS 1 with a jet to the south (Garnavich et al. 1997). Recent VLA observations found that VLA 05487 coincides with IRS 2 (Rodriguez et al. 1998). It is virtually certain that VLA 05487 is the source driving the CO outflow and associated H_2 jets; it is likely that it is also the source of the *IRAS* infrared emission (Rodriguez et al. 1998).

Figure 1 presents the CO $J = 1-0$ emission in the BIMA observations overlaid on a gray-scale H_2 image provided by Garnavich et al. (1997). A bipolar conical emission structure

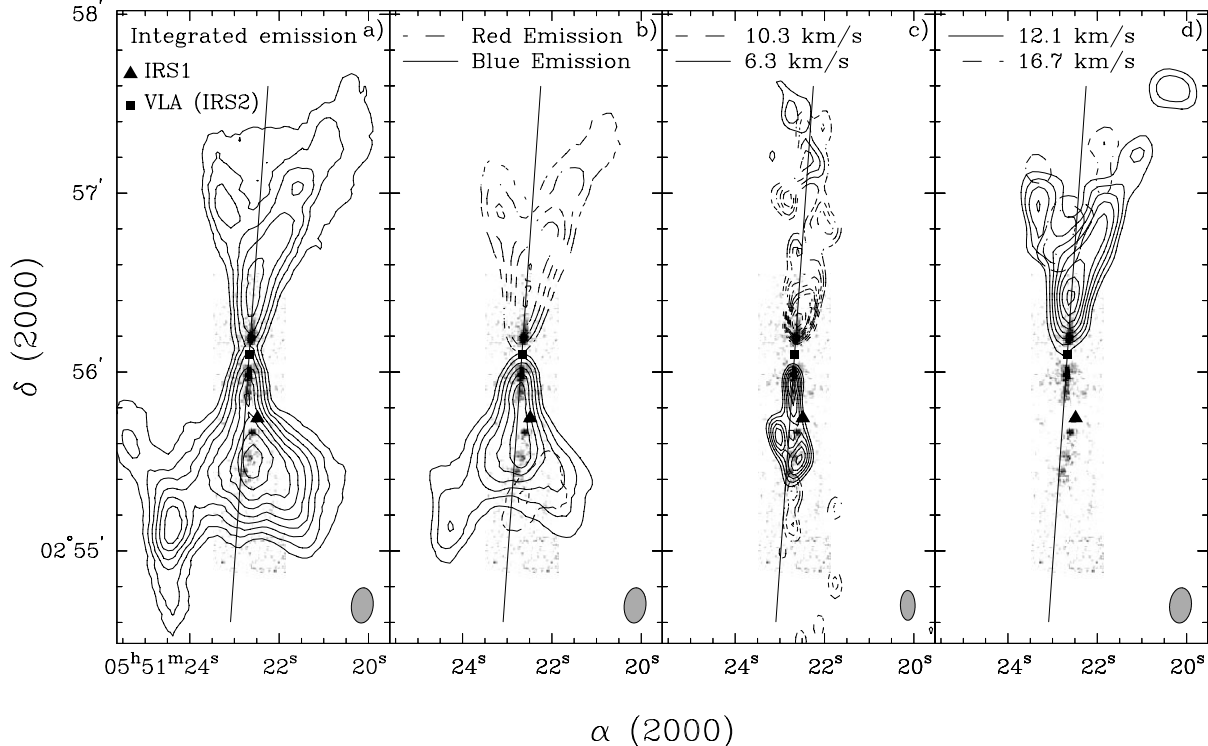


FIG. 1.—CO outflow emission for VLA 05487 in the BIMA observations overlaid on a gray-scale H_2 image provided by Garnavich et al. (1997). The line in each panel indicates the direction of the H_2 jet centered at VLA 05487 (IRS 2). (a) The CO emission integrated over the entire line profile, from 0.17 to 17.40 km s^{-1} . (b) The red emission (dashed line) integrated from 9.32 to 17.40 km s^{-1} and the blue emission (solid line) integrated from 8.30 to 0.17 km s^{-1} . (c) Channel maps to the red and blue showing the low-velocity outflow emission. (d) Two channel maps in the red wing showing how the outflow emission changes with increasing red-shifted velocity. For (a) and (b), the contours start at $10 \text{ Jy beam}^{-1} \text{ km s}^{-1}$ with a step size of $4 \text{ Jy beam}^{-1} \text{ km s}^{-1}$. For (c), the contours start at 0.6 Jy beam^{-1} with a step size of 0.2 Jy beam^{-1} . For (d) the contours start at 1.5 Jy beam^{-1} with a step size of 0.5 Jy beam^{-1} . The beam size is 11.82×7.28 for (a), (b), and (d), while 9.97×4.91 for (c).

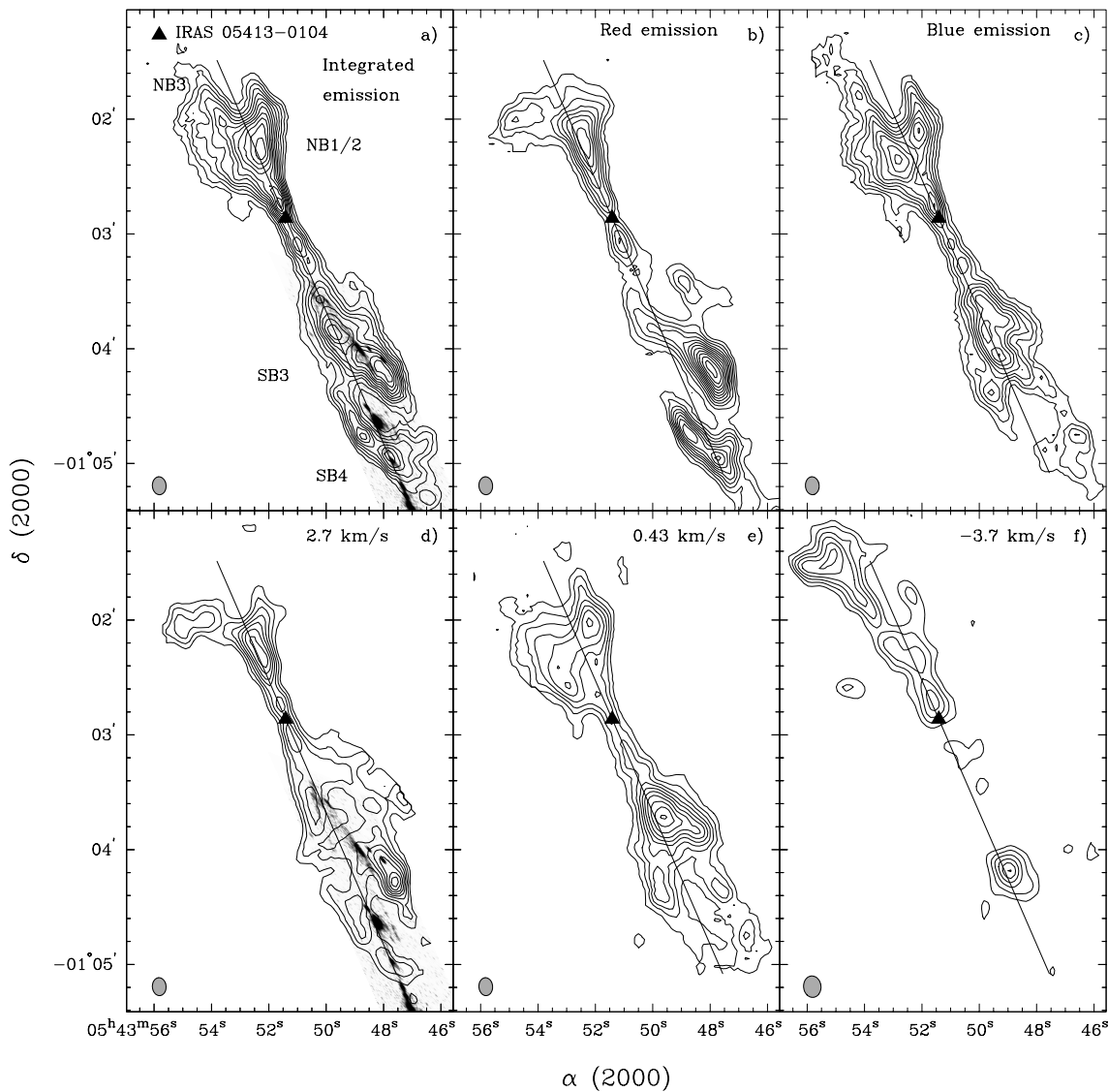


FIG. 2.—CO outflow emission of HH 212 in the BIMA observations overlaid on a gray-scale H_2 image provided by Zinnecker et al. (1998). The line indicates the direction of the H_2 jet centered at IRAS 05413–0104. The labels, NB3, NB1/2, SB3, and SB4, denote the locations of H_2 bow shocks as enumerated by Zinnecker et al. (1998). (a) The CO emission integrated from -4.2 to 5.5 km s^{-1} . This velocity range includes both the red and blue outflow emission. (b) The red emission integrated from 1.96 to 5.51 km s^{-1} . (c) The blue emission integrated from -4.5 to 1.7 km s^{-1} . (d) and (e) Channel maps at two redshifted velocities. (f) The emission at -3.7 km s^{-1} averaged over 3 km s^{-1} velocity interval to improve the signal-to-noise ratio. The contours in panel (a) start at $2 \text{ Jy beam}^{-1} \text{ km s}^{-1}$ with a step size of $2 \text{ Jy beam}^{-1} \text{ km s}^{-1}$. The contours in (b) and (c) start at $1.5 \text{ Jy beam}^{-1} \text{ km s}^{-1}$ with a step size of $1.5 \text{ Jy beam}^{-1} \text{ km s}^{-1}$. For (d) and (e), the contours start at 2.5 Jy beam^{-1} with a step size of 1 Jy beam^{-1} . For (f) the contours start at 0.6 Jy beam^{-1} with a step size of 0.3 Jy beam^{-1} . The beam size is $9''.4 \times 7''.2$.

is seen in the integrated CO emission centered at VLA 05487. The CO emission surrounds the H_2 jet from VLA 05487 and extends with the major axis aligned with the jet axis, clearly indicating that VLA 05487 is the driving source. The emission is symmetric about VLA 05487, with the red emission to the north and blue to the south. The CO outflow has the same orientation as that found by Reipurth & Olberg (1991); our maps highlight the region of the outflow close to the source. At the bottom left corner of Fig. 1a, there is a second elongated emission region extending from northeast to southwest. This emission is associated with the HH 110 knots detected by Reipurth et al. (1993) and is not related to VLA 05487. There is also a little red emission associated with IRS 1 to the south in the blue lobe of the VLA 05487 outflow (see Figs. 1b and 1c).

The cloud ambient velocity (V_{lsr}) in this region is about 8.5 km s^{-1} . Figure 1c shows two channel maps at velocities close to this velocity, one to the red (10.3 km s^{-1}) and one to the blue (6.3 km s^{-1}). The emission at these velocities forms a narrow shell structure around the jet axis. As the velocity increases to the red, the emission structure becomes conical and moves away from VLA 05487 along the jet axis, as shown in Figure 1d.

Figure 6 shows a position-velocity (PV) diagram for the CO emission cut along the jet axis, with a gray-scale image of the H_2 jet shown along the left side. The vertical dashed line indicates the ambient velocity and the horizontal dashed line indicates the driving source position. Owing to the interferometer's insensitivity to extended emission, the emission is resolved out around the ambient velocity. The

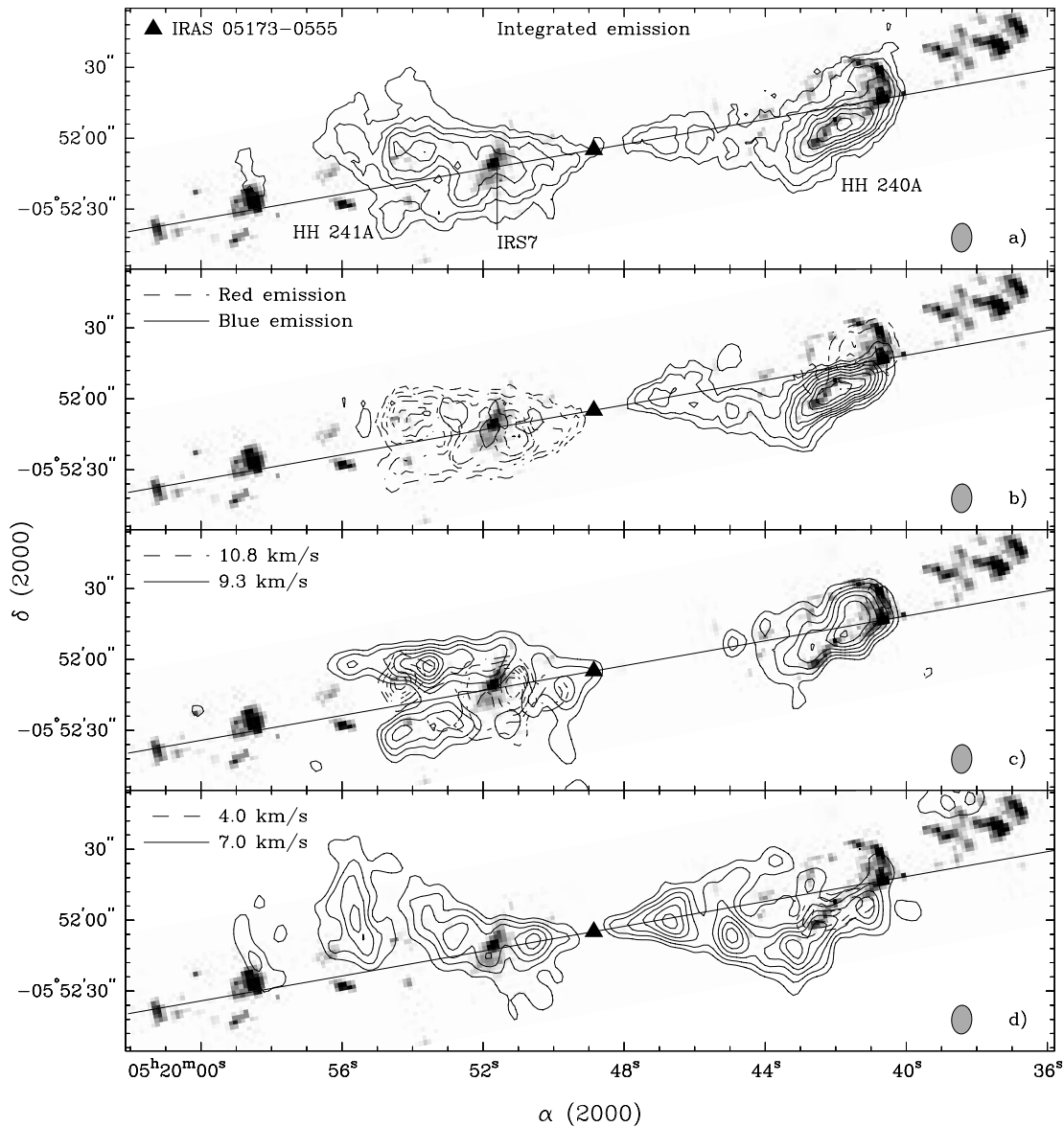


FIG. 3.—CO emission from the HH 240/241 region in the BIMA observations overlaid on a gray-scale H_2 image provided by Davis et al. (1997). The line indicates the major axis of the CO outflow. The triangle marks the position of IRAS 05173—0555. (a) The CO emission integrated over the entire line, from 13.13 to 1.70 km s^{-1} . (b) The red emission integrated from 13.13 to 9.32 km s^{-1} , and the blue emission integrated from 7.03 to 1.70 km s^{-1} . (c) and (d) Each shows two channel maps at different velocities. The velocity are given in the upper left corner of each panel. For (a) the contours start at 16 $\text{Jy beam}^{-1} \text{km s}^{-1}$ with a step size of 8 $\text{Jy beam}^{-1} \text{km s}^{-1}$. For (b), the contours start at 10.0 $\text{Jy beam}^{-1} \text{km s}^{-1}$ with a step size of 5 $\text{Jy beam}^{-1} \text{km s}^{-1}$. For panels (c) and (d), the contours start at 4.5 Jy beam^{-1} with a step size of 1.8 Jy beam^{-1} . The beam size is $12''.11 \times 8''.53$.

northern half of the PV diagram shows a tilted parabolic structure opening up from the source. This structure is clearest in the north lobe of the outflow because it is not contaminated by the outflow associated with IRS 1. The PV diagram also shows that the maximum velocity increases with increasing projected distance along the jet axis. Since the CO emission appears as shell structures in the channel maps, the emission mostly arises from an excavated shell. In the southern lobe, the emission near the source peaks around the H_2 jet and is associated with a broad range of velocities.

3.2. HH 212

HH 212 is a highly symmetric two-sided H_2 jet system driven by IRAS 05413—0104 in the Orion molecular cloud (Zinnecker, McCaughrean, & Rayner 1998). The jet system

is about $240''$ long (0.6 pc), with matched pairs of H_2 knots and bow shock structures along the jet axis. IRAS 05413—0104 itself is a low-mass ($0.4 M_\odot$), cold (≈ 30 K), low-luminosity ($14 L_\odot$) source (Zinnecker et al. 1992). It is argued to be a class 0/I source in terms of the ratio of the millimeter-wave luminosity to the bolometric luminosity (Claussen et al. 1998). It is associated with a strong 1.3 cm water maser moving with velocity of 64 km s^{-1} (Wouterloot & Walmsley 1986; Claussen et al. 1998), highly collimated shocked SiO emission along the jet, and an extended $C^{18}O$ “disk” or “torus” perpendicular to the jet axis (Marvel, McCaughrean, & Sargent 2000, in preparation). Recent observations in NH_3 (1,1) also revealed a rotating edge-on flattened VLA ammonia core with an axis ratio of 2:1 toward the driving source (Wiseman et al. 1999). Based on the relative magnitude of

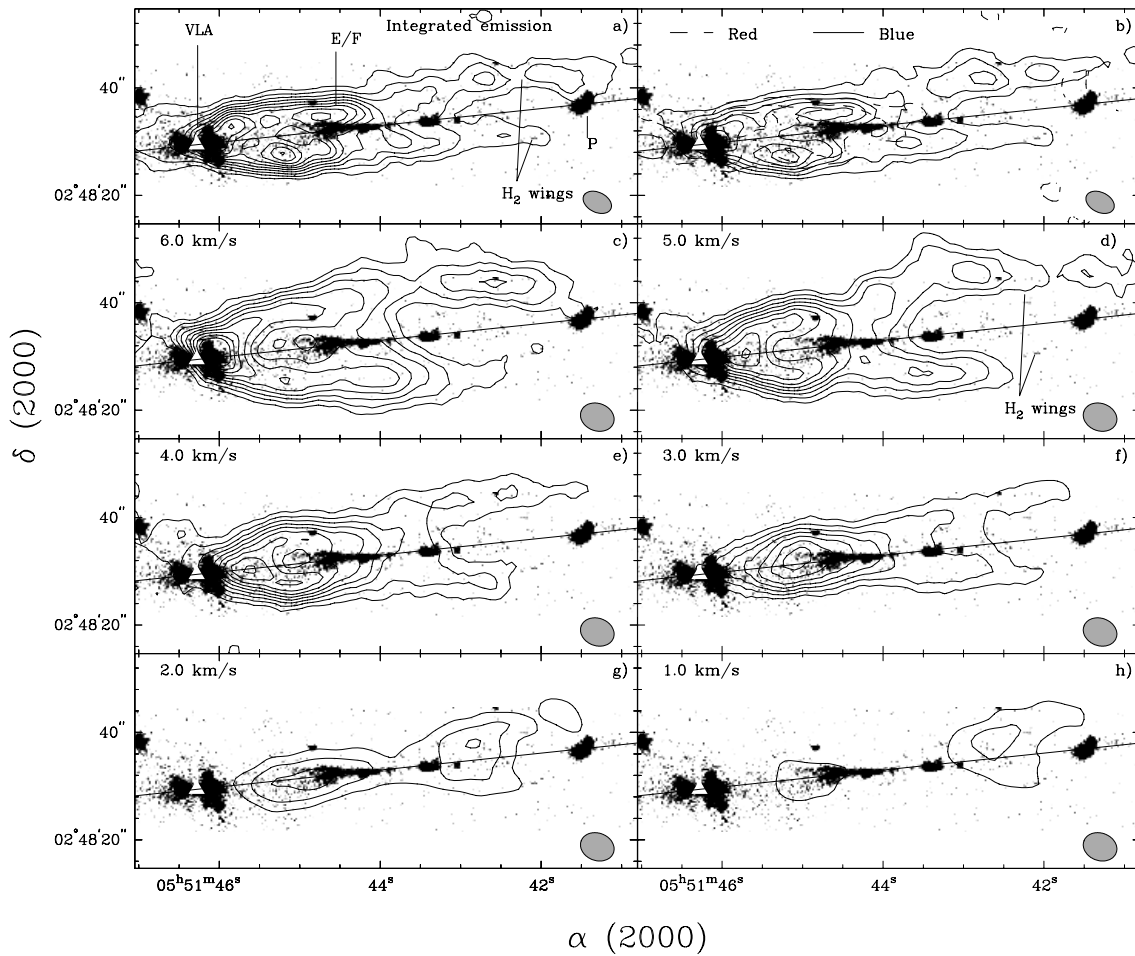


FIG. 4.—CO emission for the HH 111 region on top of a gray-scale H_2 (+continuum) image provided by Coppin et al. (1998), with the line indicating the jet axis. The gray-scale blobs within $\pm 5''$ from the VLA source are continuum; the other emission is from H_2 . (a) The CO emission integrated over the entire line, from -1 to 12 km s^{-1} . The line labeled VLA points to the central source. The label E/F indicates the location of the bow shocks denoted by Reipurth et al. (1992). (b) The red emission integrated from 9 to 12 km s^{-1} and the blue emission integrated from -1 to 7 km s^{-1} . (c)–(h) are the channel maps at six velocities increasing to the blue, showing the two structures of the emission. For (a) and (b) the contours start at $1.5 \text{ Jy beam}^{-1} \text{ km s}^{-1}$ with a step size of $1.5 \text{ Jy beam}^{-1} \text{ km s}^{-1}$. For (c)–(h) the contours start at 0.5 Jy beam^{-1} with a step size of 0.5 Jy beam^{-1} . The beam size is $5''.6 \times 3''.7$ for (a) and (b), while $6''.4 \times 5''.1$ for (c)–(h).

the proper motions and radial velocities of the water masers, the outflow lies within 5° to the plane of the sky (Claussen et al. 1998). This inclination makes it an excellent system to investigate the transverse kinematics of the molecular outflow.

Figure 11 presents the CO emission from the region based on the FCRAO observations. The gray-scale image shows the emission integrated over all velocity channels, outlining the distribution of the ambient material (velocities from -4.2 to 5.5 km s^{-1}). The contours show the emission in the blue wing (velocities from 1.0 to -4.5 km s^{-1}). Since the outflow lies close to the plane of the sky, the blue wing emission is almost equally strong in both lobes. As can be seen, the north lobe of the outflow ends near the cloud edge. We do not show the red wing because it is heavily contaminated by cloud emission. Figure 12 shows the spectra for the region around the driving source. There are three peaks in the FCRAO spectrum with the highest at velocity of 9 km s^{-1} and the lowest at 1.8 km s^{-1} . The systematic velocity for the outflow is about 1.8 km s^{-1} , as seen in the BIMA spectrum. In the BIMA observations, the cloud emission is resolved out, allowing us to see the outflow emission in both the red and blue wings. The flux in the blue wing is similar

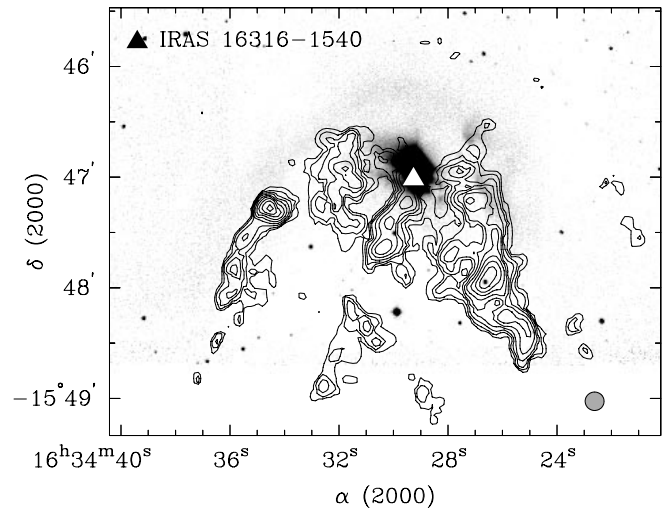


FIG. 5.—CO emission for RNO 91 integrated from -0.78 to -1.28 km s^{-1} on top of a K -band continuum image from Hodapp (1994). The CO map is a maximum entropy deconvolution of the joint FCRAO and BIMA data. The contours start at 2 Jy beam^{-1} with a step size of 1 Jy beam^{-1} . The beam size is $10'' \times 10''$.

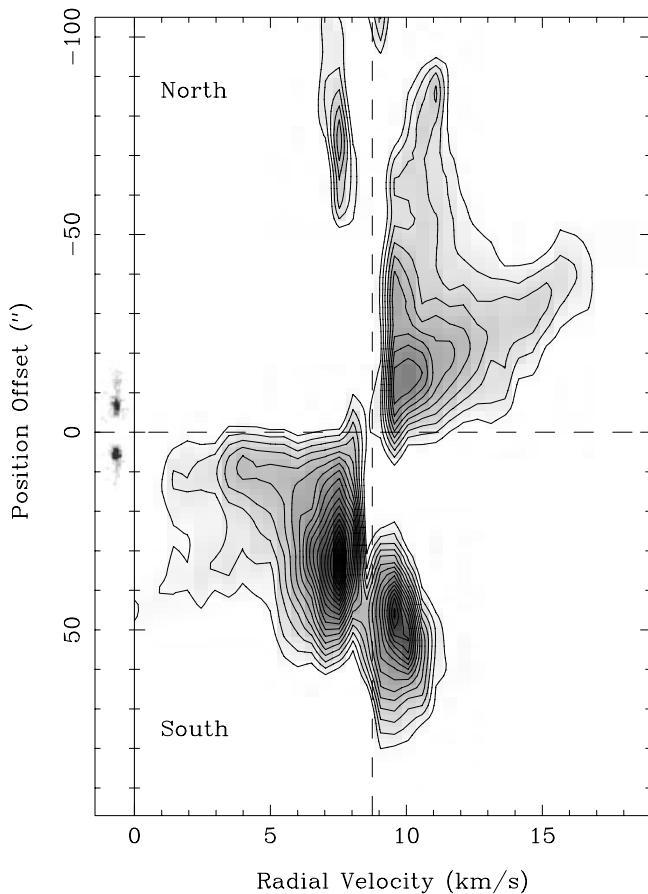


FIG. 6.—PV diagram of the VLA 05487 outflow cut along the jet axis, with the H_2 image of the jet displayed along the left side. Vertical dashed line indicates the ambient velocity. Horizontal dashed line indicates the driving source position. The contours start at 2.5 Jy beam^{-1} with a step size of 1 Jy beam^{-1} . The emission near ambient velocity is resolved out by the interferometer.

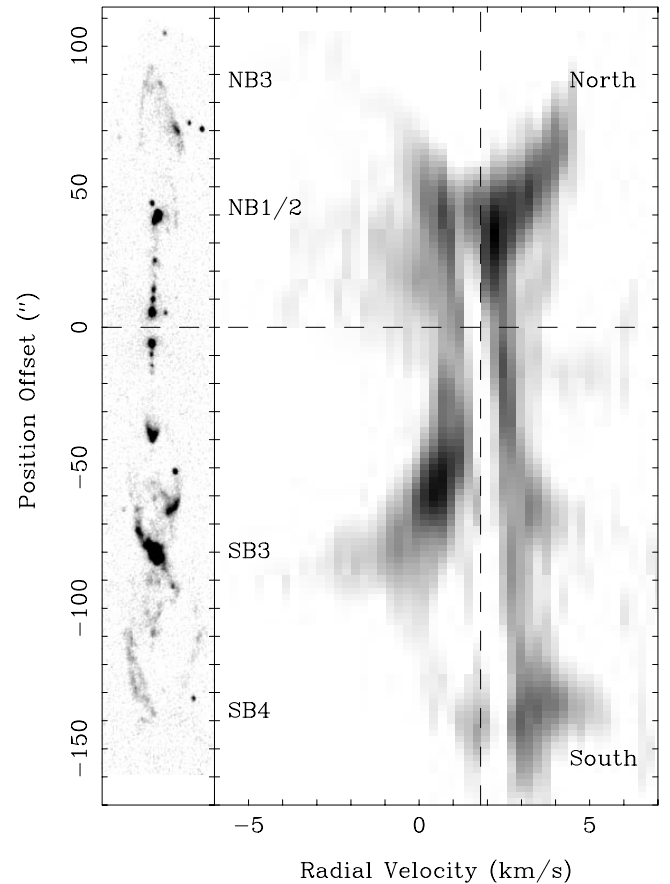


FIG. 7.—PV diagram of the HH 212 outflow cut along the jet axis, with the H_2 image of the jet along the left side. The vertical dashed line indicates the ambient velocity. The horizontal dashed line indicates the driving source position.

in the FCRAO and BIMA data, indicating that the BIMA observations detect all the emission in the line wings. However, the flux at the line center is mostly resolved out in the BIMA data.

Figure 2 presents the BIMA observations overlaid on a gray-scale H_2 image provided by Zinnecker et al. (1998). The integrated CO emission is well aligned with the H_2 jet and shows a striking morphological relation with the H_2 emission. In the south, the CO emission forms a hollow lobe structure with the tip around the bow shock SB4 (following the notation of Zinnecker et al. 1998). In the north, the CO emission peaks near the bow shock NB 1/2 and connects to the bow shock NB3 (see the blue emission). Since the outflow is almost in the plane of the sky, the red and blue emission is distributed equally in the north and south lobes; however, there are significant asymmetries in the emission. In the south, the blue and red emission appear on the opposite sides of the major axis in such a way that they complement each other. In the north, part of the blue emission shifts to the east, consistent with a wisp swept up along the blue side of the outflow detected in the NH_3 (1,1) (Wiseman et al. 1999). Again in the north, the brightest blue and red emission are spatially distinct.

Figures 2d and 2e present two channel maps near the ambient velocity, one to the red (2.7 km s^{-1}) and one to the

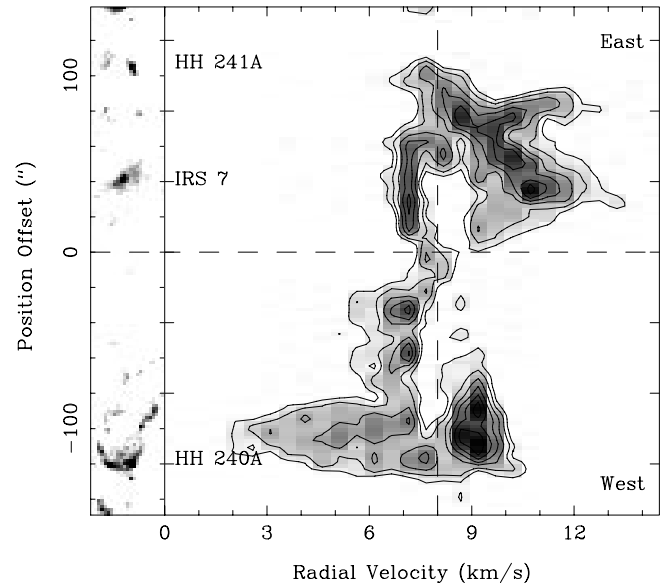


FIG. 8.—PV diagram of the HH 240/241 outflow cut along the major axis, with the H_2 image of the jet along the left side. The vertical dashed line indicates the ambient velocity. The horizontal dashed line indicates the driving source position. Contours start at 2.4 Jy beam^{-1} with a step size of 1.2 Jy beam^{-1} .

blue (0.43 km s^{-1}). Figure 2f shows the emission at -3.7 km s^{-1} to highlight the association of CO emission with the bow shocks to the northeast. These panels show that the CO emission is not only associated with the most distant bow shock structures, but also with the inner bow shock structures and knots. In the south lobe, the CO emission is not only surrounding bow shock SB4 but also SB3; in fact, both the bow shocks SB3 and SB4 are associated with their own CO structures. Note that some of the CO emission near bow shock SB4 is connected to the end of bow shock SB3. In the north lobe, the CO emission not only forms a shell structure around bow shock NB3, but also peaks at the inner shocks and knots (see Fig. 2f).

A PV diagram of the CO emission along the jet axis is shown in Figure 7, with the lines indicating the source position and the ambient velocity. The diagram shows that the CO outflow has different kinematics from VLA 05487. The major bow shock structures, including inner ones, show significant features in the PV diagram. The diagram shows a series of convex velocity spur structures with ends near the major bow tips (NB3, SB3 and SB4), indicating a broad range of velocities near the tips, with the maximum transverse motion increasing toward the tips. Near the source, there are similar faint structures associated with the inner bow shock structures and knots.

3.3. HH 240/241

HH 240/241 is a pair of Herbig-Haro objects (Cohen 1980; Bohigas, Persi, & Tapia 1993), which in the infrared H_2 lines form a spectacular bipolar flow at a distance of 460 pc in the Orion molecular cloud L 1634 (Davis et al. 1997). It consists of a series of well-defined H_2 bow shocks distributed symmetrically about the central driving source, IRS 05173–0555. It extends east-west with a total length of $6'$, corresponding to a projected length of 0.8 pc. The *IRAS* source has a bolometric luminosity of $17 L_\odot$ and may be in transition between the class 0 and class I phases (Hodapp &

Ladd 1995). The 1.3 mm survey of Reipurth et al. (1993) detected a cool dust emission toward the *IRAS* source, and CO $J = 3-2$ spectra indicate that it is the driving source of the flow (Davis et al. 1997). There is a second independent flow associated with IRS 7, located $50''$ to the east of the *IRAS* source (Hodapp & Ladd 1995; Davis et al. 1997). It extends to the northwest and southeast, but judging from the symmetry of the CO lobes, it does not appear to significantly affect the structure and kinematics of the outflow associated with IRS 05173–0555.

Figure 13 presents the CO emission from the region based on FCRAO observations. The gray-scale image shows the emission integrated over the line center, outlining the distribution of the ambient material. The contours show the red and blue wing emission. As can be seen, the red and blue wing emission are on opposite sides of the outflow, with the red wing emission ending near the cloud edge. Figure 14 shows spectra from the FCRAO and BIMA data. The ambient velocity in this region is about 8 km s^{-1} . The flux in the line wings is similar in the FCRAO and BIMA data, indicating that the BIMA observations have detected all the emission in the line wings. However, the flux in the line center is almost completely resolved out in the BIMA data.

Figure 3 shows the CO emission in the BIMA observations overlaid on a gray-scale H_2 image from Davis et al. (1997). The integrated CO emission (Fig. 3a) shows a clear relationship between the CO and H_2 emission. In the east lobe, the CO emission forms a hollowed shell structure pointing toward the H_2 bow shock structures further to the east. In the west lobe, the CO emission curves around the big bow shock HH 240A. There are smaller bow shock structures beyond this bow shock, however, almost no CO emission is detected there. Figure 3b presents the total red and blue emission. As can be seen, most of the red emission is to the east, while the blue is to the west.

Figures 3c and 3d show the structure of the red emission and blue emission, respectively, in two velocity channels. In

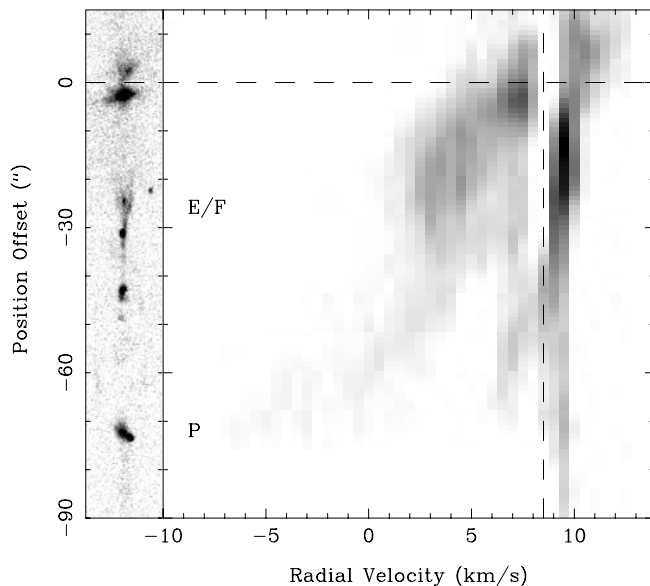


FIG. 9.—PV diagram of the HH 111 outflow cut along the jet axis, with the H_2 (+continuum) image of the jet along the left side. The vertical dashed line indicates the ambient velocity. The horizontal dashed line indicates the driving source position. The labels E/F and P indicate the positions of bow shocks (Reipurth et al. 1992)

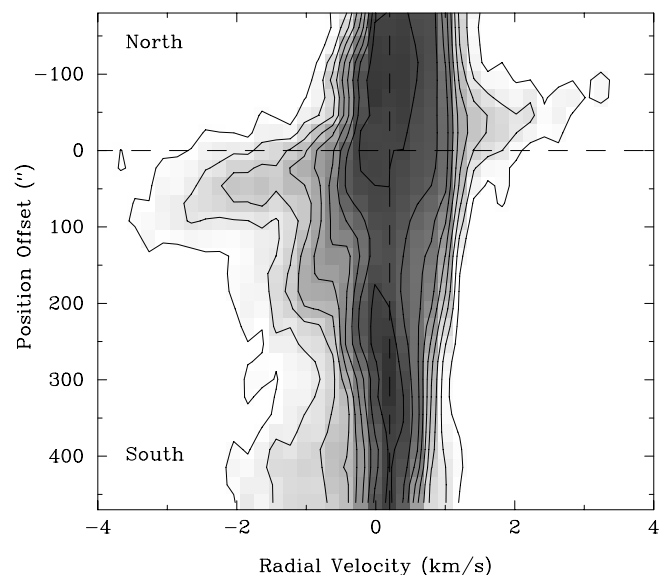


FIG. 10.—PV diagram of the RNO 91 outflow cut along the major axis of the CO emission. The vertical dashed line indicates the ambient velocity. The horizontal dashed line indicates the driving source position. Contours start at 0.5 K with a step size of 0.5 K.

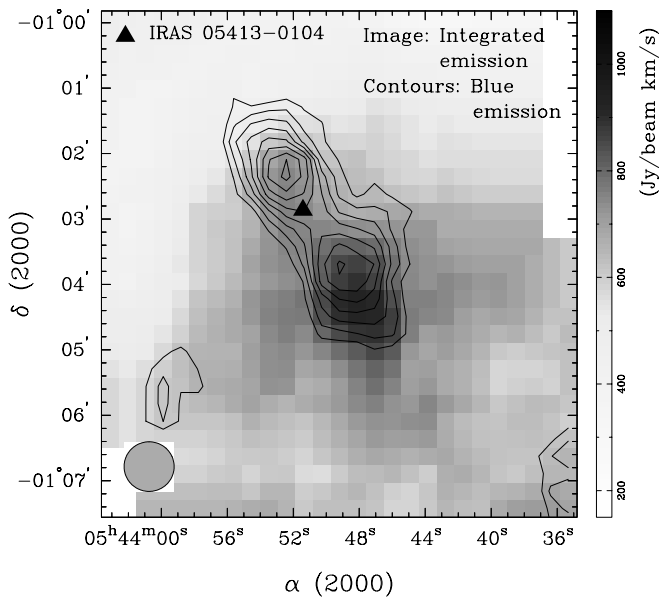


FIG. 11.—CO emission for the HH 112 region from the FCRAO observations. Gray-scale image is the emission integrated from -4.2 to 5.5 km s^{-1} . The gray-scale wedge along the right side indicates the values for the gray-scale image. The contours show the emission in the blue wing, integrated from 1 to -4.5 km s^{-1} . The contours start at $30 \text{ Jy beam}^{-1} \text{ km s}^{-1}$ with a step size of $10 \text{ Jy beam}^{-1} \text{ km s}^{-1}$. The beam size is $46''$.

these channel maps, shell structures are clearly seen on both sides of the outflow. Moreover, in the east lobe, the emission at higher velocity resides inside that at lower velocity. In the west lobe, the bow shock region is associated with the emission from the lower red (Fig. 3c) to higher blueshifted velocities (Fig. 3d), indicating a broad range of velocity near the bow shock HH 240A. The CO emission at 9.3 km s^{-1} even shows a structure similar to the bow shock HH 240A.

Figure 8 shows the PV diagram for the CO emission cut along the jet axis. The dashed lines indicate the source position and ambient velocity. In the blue emission, a curved structure is seen in the western lobe ending at bow shock HH 240A. The bow shock is associated with a broad range in velocity and the velocity increases toward the bow tip, as seen in the channel maps (see Figs. 3c and 3d). The PV structure in the east lobe is more complicated. The velocity structure seems to be affected by IRS 7, the very faint H_2

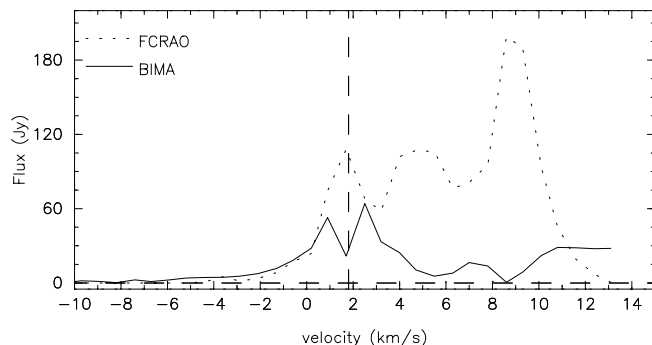


FIG. 12.—CO spectra of HH 212 in the FCRAO (dotted line) and BIMA (solid line) observations for the region around the driving source. The BIMA spectrum was created by summing over a box with area equal to the FCRAO beam. The two spectra are directly comparable in janskys.

emission structures at $80''$, as well as the bow shock HH 241A.

3.4. HH 111

Located in L1617, one of the Orion B clouds, HH 111 is about 460 pc away. It consists of a series of knots and bow shock structures in $\text{H}\alpha$, $[\text{S II}]$ (Reipurth et al. 1997b, 1999) and H_2 (Gredel & Reipurth 1994; Coppin, Davis, & Micono 1998) emission. Recently, it was found that HH 113 and HH 311 are part of the same system, making the HH 111 flow about 7.7 pc in extent (Reipurth, Bally, & Devine 1997a). The flow is inclined about 10° away from the plane of the sky, as derived from proper motion and radial velocity observations (Reipurth, Raga, & Heathcote 1992). CO outflow emission has been found in this region (Reipurth & Olberg 1991), with the low-velocity gas forming a hollow tubular structure surrounding the optical jet (Reipurth & Cernicharo 1995; Nagar et al. 1997). Cernicharo & Reipurth (1996) also discovered three very high velocity molecular clumps in CO $J = 2-1$ to the west of the low-velocity molecular flow and identified them as CO bullets propagating through a low-density medium. The driving source for this system is a class I source IRAS 05491 + 0247 with luminosity of $25 L_\odot$. This IRAS source was detected in VLA observations at 3.6 cm HH 111 VLA, HH 111 VLA, Rodriguez & Reipurth (1994); Reipurth et al. (1999) and found to be associated with a rotating molecular disk perpendicular to the jet axis (Yang et al. 1997).

Figure 15 shows the CO emission from the overall region. The gray-scale image presents the emission integrated over the line center, outlining the distribution of the ambient material. The contours show the red and blue wing emission from the outflow. The ambient velocity CO emission peaks in the area of IRAS 05491 + 0247 and falls off strongly in all directions except to the northeast. The red and blue wing emission is on opposite sides with the blue wing emission

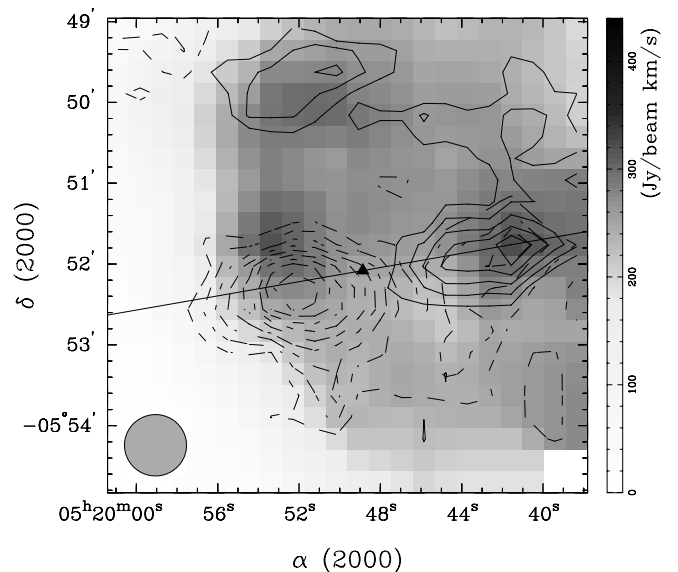


FIG. 13.—CO emission in the HH 240/241 region based on FCRAO observations. Gray-scale image is the emission integrated over the line center, from 7.2 to 8.7 km s^{-1} . Solid contours show the blue emission integrated from 2.2 to 6.7 km s^{-1} and dashed contours show the red emission integrated from 9.2 to 13.7 km s^{-1} . The contours start at $36 \text{ Jy beam}^{-1} \text{ km s}^{-1}$ with a step size of $12 \text{ Jy beam}^{-1} \text{ km s}^{-1}$. The triangle is the driving source IRAS 05173-0555. The beam size is $46''$.

ending near the edge of the cloud core as previously shown. Notice that part of the red wing emission is oriented NE-SW and associated with another H_2 flow, HH 121. Figure 16 shows CO spectra for the western lobe. The ambient velocity of this system is about 8.5 km s^{-1} . The flux in the blue wing is similar in the FCRAO and BIMA data, indicating that the BIMA maps contain nearly all of the CO flux in the blue wing. The emission in the red wing appears to be more extended and is not completely represented in the BIMA data.

Figure 4 presents the CO emission on top of a gray-scale H_2 (+ continuum) image provided by Coppin et al. (1998). The integrated CO emission shows an elongated CO shell structure extending out to bow shock P and surrounding the H_2 emission. The CO emission structure is slightly pinched near the bow shocks E/F, with the CO emission

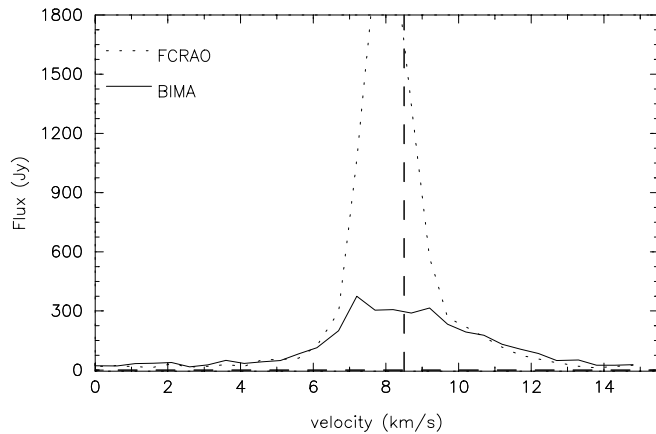


FIG. 14.—CO spectra of HH 240/241 in the FCRAO (dotted line) and BIMA (solid line) observations for the outflow region. The BIMA spectrum was created by summing over a box with area equal to the FCRAO beam. The two spectra are directly comparable in janskys.

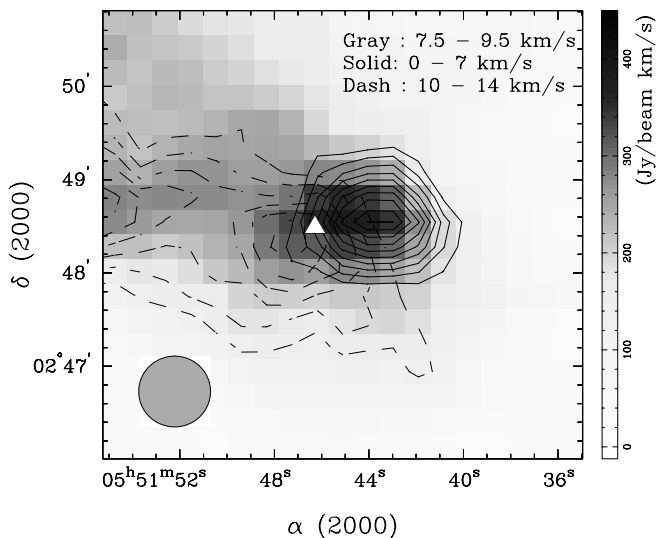


FIG. 15.—CO emission from the HH 111 region in the FCRAO observations. Gray-scale image is the emission integrated over the line center from 7.5 to 9.5 km s^{-1} . Solid contours show the blue emission integrated from 0 to 7 km s^{-1} and dashed contours show the red emission integrated from 10 to 14 km s^{-1} . The contours start at $30 \text{ Jy beam}^{-1} \text{ km s}^{-1}$ with a step size of $10 \text{ Jy beam}^{-1} \text{ km s}^{-1}$. The white triangle is the driving source HH 111 VLA (Rodriguez & Reipurth 1994). The beam size is $46''$.

upstream (east) of bow shocks E/F stronger than that downstream. As seen in the Fig. 4b, the red and blue emission overlaps in the region close to the source, with the blue emission stronger than the red emission. However, only blue emission is detected beyond bow shocks E/F. Figure 4c–4h present channel maps with velocity increasing to the blue. At a velocity of 6 km s^{-1} , the CO emission forms a smooth shell structure surrounding the H_2 emission. As the velocity increases to the blue, the CO emission structure breaks into two structures, one peaking around the bow shocks E/F and the other upstream of the bow shock P (see Fig. 4h). The bow shocks E/F coincide with the surface of the ambient cloud core (Reipurth et al. 1992; Cernicharo & Reipurth 1996).

Figure 9 presents the PV diagram of the CO emission along with the gray-scale H_2 (+ continuum) image. A tilted parabolic PV structure is found to be associated with the emission structure inside $30''$ offset from the driving source (as seen by Nagar et al. 1997). The velocity increases toward bow shocks E/F where the cloud core ends. A second PV structure is seen associated with the outer CO emission. The PV structure extends from inside the inner tilted parabola, and ends near the bow shock P. This PV structure can not be traced back all the way back to the source. The eastern end of this PV structure is associated with a broad range of velocities, qualitatively similar to the PV structure in HH 212.

3.5. RNO 91

RNO 91 is about 160 pc away in the L 43 molecular cloud. The driving source is a class II/III embedded T Tauri star IRAS 16316–1540 in a transition phase between an embedded and optical star (André & Montmerle 1994). It has a bolometric luminosity of $4.3 L_{\odot}$ (Terebey, Chandler, & Andre 1993) and a mass of about $0.5 M_{\odot}$ (Levreault 1988). It illuminates a reflection nebula RNO 91 (Cohen 1980), and the blue U-shaped lobe of the CO outflow fits precisely into the bay of the nebula (Mathieu et al. 1988). Recent observations have found the $H_2 v=1-0 \text{ S}(1)$ line emission extending spatially up to $9''$ in the north-south direction (Kumar, Anandaramo, & Davis 1999). CO $J=2-1$ observations toward the outflow show a weak jetlike low-

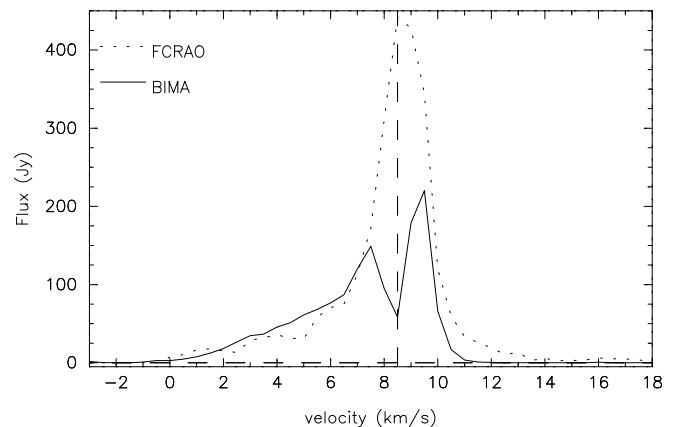


FIG. 16.—CO spectra of HH 111 in the FCRAO (dotted line) and BIMA (solid line) observations for the western lobe of the outflow. The BIMA spectrum was created by summing over a box with area equal to the FCRAO beam. The two spectra are directly comparable in janskys.

velocity emission along the major axis up to about $500''$ away from the driving source (Bence et al. 1998).

Figure 17 shows the CO $J = 1-0$ emission based on FCRAO maps. The integrated emission clearly shows a limb-brightened U-shaped blue lobe to the south of IRAS

16316–1540. There is very little red emission in the southern lobe, indicating that the outflow is tilted away from the plane of the sky. The blue lobe is not symmetric about the driving source: the centroid of the outflow emission seems to curve eastward with increasing distance from

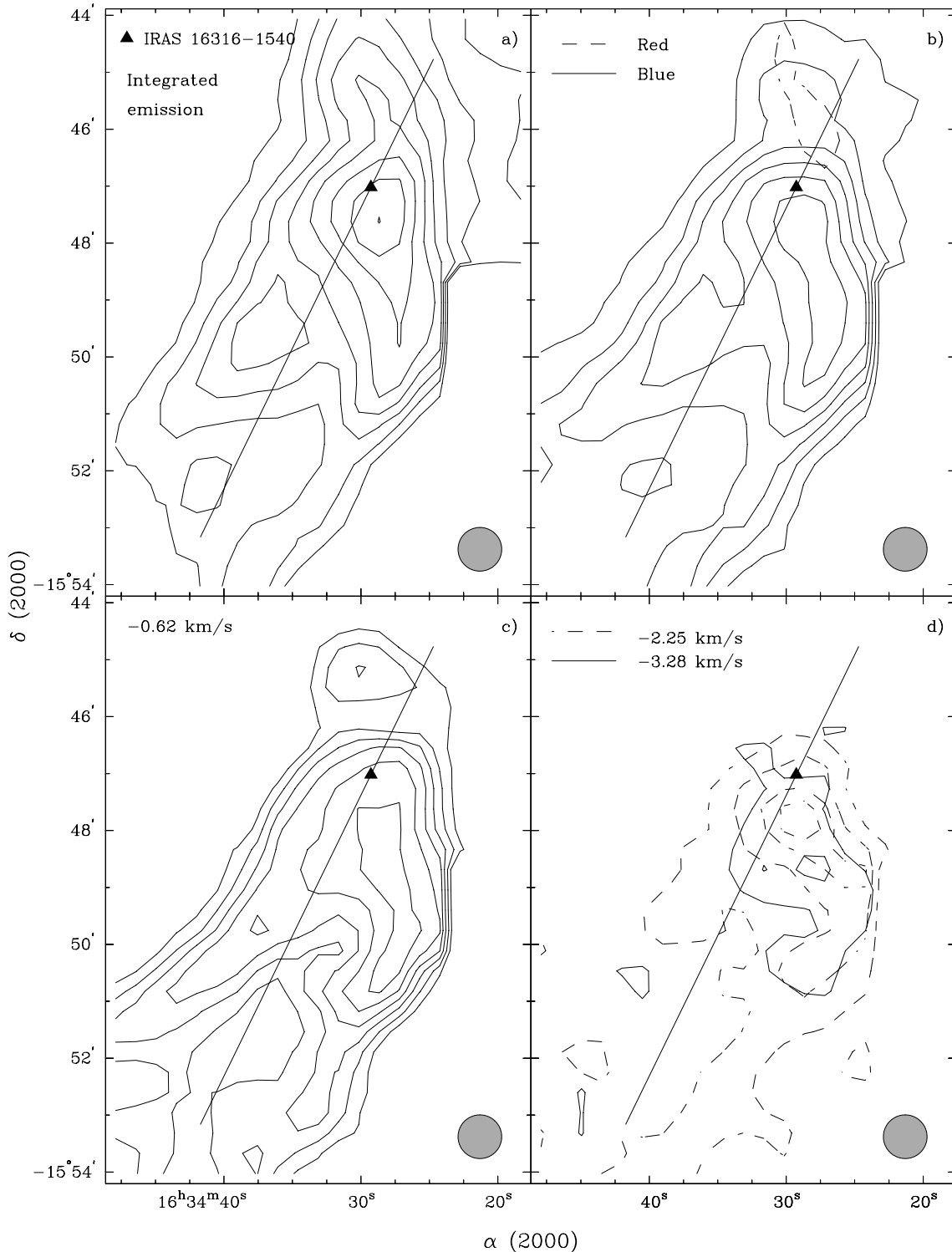


FIG. 17.—CO emission for the RNO 91 region in the FCRAO observations. The line indicates the averaged major axis of the outflow. The triangle indicates the location of the driving source, IRAS 16316–1540. (a) The CO emission integrated over the entire line, from -5 to 5 km s^{-1} . (b) The red emission integrated from -5 to 0.5 km s^{-1} , and the blue emission integrated from 0 to 5 km s^{-1} . (c) and (d) show channel maps at different velocities. For (a) the contours start at 6 K km s^{-1} with a step size of 1 K km s^{-1} . For (b), the contours start at 2 K km s^{-1} with a step size of 1 K km s^{-1} . For (c) the contours start at 1.2 K with a step size of 0.4 K . For (d) the contours start at 0.35 K with a step size of 0.4 K . The beam size is $46''$.

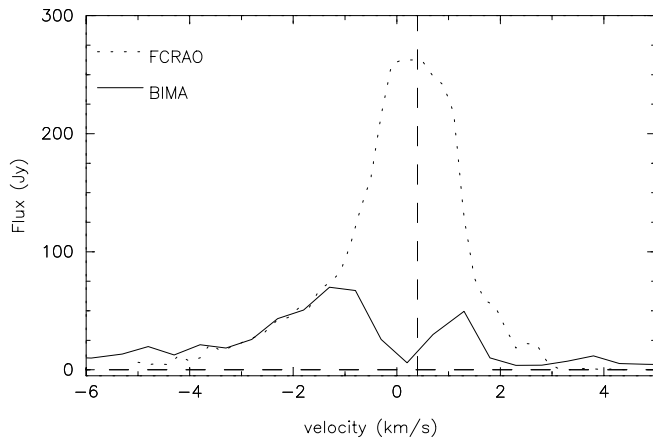


FIG. 18.—CO spectra for RNO 91 in the FCRAO (dotted line) and BIMA (solid line) observations for the region around the driving source. The BIMA spectrum was created by summing over a box with area equal to the FCRAO beam. The two spectra are directly comparable in janskys.

the source. This could indicate that there is an interaction with ambient material that guides the orientation of the outflow. Alternatively, it could be that the intrinsic outflow axis is changing with time as a result of precession in the exciting source. The ambient velocity of this system is about 0.5 km s^{-1} . Figs. 17c and 17d show the CO emission with velocity increasing to the blue. At a velocity close to the ambient velocity, the emission structure forms a shell structure. With increasing velocity, the emission moves away from the source. The emission structure in CO $J = 1-0$ is similar to that observed in CO $J = 2-1$ by Bence et al. (1998), the average intensity ratio of CO $J = 2-1$ to CO $J = 1-0$ is found to be about 2, indicating that the excited temperature for the CO outflow is 20–50 K, and the emission is not optically thick in the $J = 1-0$ transition.

Figure 18 presents CO spectra for the region around the source. In the BIMA data, the flux in the line core is almost resolved out. However, the BIMA data contain all of the CO flux in the blue wing. The red wing emission, which is near the edge of the BIMA primary beam, is not well represented in the BIMA observations. The BIMA data was combined with the FCRAO data to recover the large scale structure of the CO emission. Figure 5 shows the combined CO emission integrated from -0.78 to -1.28 km s^{-1} on top of a K -band continuum image from Hodapp (1994). The CO emission fits into the bay of the reflection nebula and traces the wall structure of the blue outflow lobe. Little CO emission is detected to the north of the driving source, perhaps because of CO opacity in ambient material.

TABLE 2
MAXIMUM COLUMN DENSITY AND MASS^a

Outflow	Column Density (10^{21} cm^{-2})	Mass ($10^{-1} M_{\odot}$)
VLA 05487	1.5	1.5
HH 212	1.4	2.0
HH 240/241	2.4	2.2
HH 111	2.5	0.6
RNO 91	1.3	1.1

^a Assuming CO emission is optically thin and $T_{\text{ex}} = 50 \text{ K}$.

Figure 10 shows the PV diagram of the CO emission along the major axis. Dashed lines indicate the source position and the ambient velocity. The arms extending from the source position in the diagram indicate that the velocity increases with increasing distance in both the north and south lobes for the first $100''$ from the source. There are two other weak arms in the south lobe, one extending from the source to about $200''$ tracing the on-axis emission feature in the Figure 5, and one extending at a position of about $400''$ south.

3.6. Outflow Density and Mass

Assuming that the CO emission is optically thin, that the excitation temperature is 50 K (a typical temperature for the outflow associated with a low mass star; Fukui et al. 1993), and the CO abundance is 8.5×10^{-5} , we have calculated the observed peak column density and mass for all the outflows. Results are shown in Table 2. Because of the absorption of the ambient cloud and the possibility that ^{12}CO is optically thick in portions of the flow, the values in the table are lower limits of the true values. As seen from the table, the peak H_2 column densities are around 10^{21} cm^{-2} . The outflow masses are of order $10^{-1} M_{\odot}$. The average density can be estimated by integrating column density over the whole outflow and dividing it by the width of the outflow. The average density is found to be $\sim 10^4 \text{ cm}^{-3}$. If the CO outflow material is concentrated in a thin shell rather than a filled lobe, the true density in the shell could be an order of magnitude larger.

3.7. Summary of Observations

In our observations, central cavities are present in outflows with different collimations in different evolutionary stages. The CO emission commonly forms shell structures around the outflow axis. In the outflows that are associated with H_2 bow shock structures, the bright CO emission is commonly associated with the bow shocks, showing a striking morphological coincidence between the CO and H_2 emission. In these sources, CO emission can be found around both inner and outer bow shocks. There are two primary structures identified in PV diagrams along the outflow axis: (1) a parabolic structure (e.g., VLA 05487 and HH 111), and (2) a velocity spur structure associated with a bow shock (e.g., HH 212, HH 240/241 and HH 111). More than one type of PV structure can appear in a single outflow, e.g., HH 111.

4. DISCUSSION

4.1. Driving Mechanisms of CO Outflows

H_2 emission is always considered to trace the recently shocked hot material because of its high-excitation temperature (typically 2000 K) and short cooling time scale (a few years) (McKee et al. 1987). CO emission, on the other hand, traces the cooled shocked material (20–100 K). The combination of H_2 images and CO mapping thus provides us with a more complete picture of the structure and kinematics of the molecular outflows, allowing us to investigate the driving mechanism of molecular outflows.

Currently, the two most promising models for driving the molecular outflows are the jet-driven bow shock model and the wind-driven-shell model. In the following sections we will first present our best example of a jet-driven outflow, HH 212, and of a wind-driven outflow, VLA 05487. We will

then discuss the other three systems in the context of these models.

4.1.1. A Jet-driven Bow Shock Model for HH 212

In HH 212, the CO emission is found close to the H_2 bow shocks. This morphological relation between the CO and H_2 emission has also been found in recent observations of other molecular outflows: L 1448 (Bachiller et al. 1995), RNO 43 (Bence, Richer, & Padman 1996), L 1157 (Gueth et al. 1996), and HH 211 (Gueth & Guilloteau 1999). This morphology can be produced in simulations of a jet propagating into ambient material (Suttner et al. 1997; Smith et al. 1997), suggesting that the CO emission is arising in material entrained through jet-driven bow shocks such as those traced by the H_2 emission.

In the jet-driven bow shock model, when a jet propagates into ambient material, a bow shock is formed at the head of the jet. The bow shock interacts with the ambient gas, forming a dense shell of shocked gas around the jet, which is seen as the molecular outflow. Recent simulations (e.g., Smith et al. 1997) of a radiative heavy molecular jet propagating into a stationary ambient material of uniform density show that the shape of the shell structure roughly follows $z \propto R^s$ with s about 2.4, where z is along the jet axis and R is orthogonal, and $(z, R) = (0,0)$ is at the head of the bow shock (see Fig. 19). The velocity of the material in the shell can be derived by dividing the accumulated momentum flow rate along the shell surface by the mass inflow rate of the ambient material (Smith et al. 1997). From the bow apex to the wings, the shock becomes more oblique and the velocity decreases. This model has been used to explain the molecular outflow NGC 2264G quite successfully (Smith et al. 1997). PV diagrams along the jet axis for the model at four different inclinations to the plane of the sky, i , are presented in Figure 20 for a jet velocity of 100 km s^{-1} . The diagrams are calculated using the algorithm in the appendix of Smith et al. (1997). In the figure, the PV diagrams show that the jet-driven bow shock is always associated with a broad range of velocities near the bow tip while there is a small and almost constant velocity in the bow wings, producing a spur structure in the PV diagram along the jet axis.

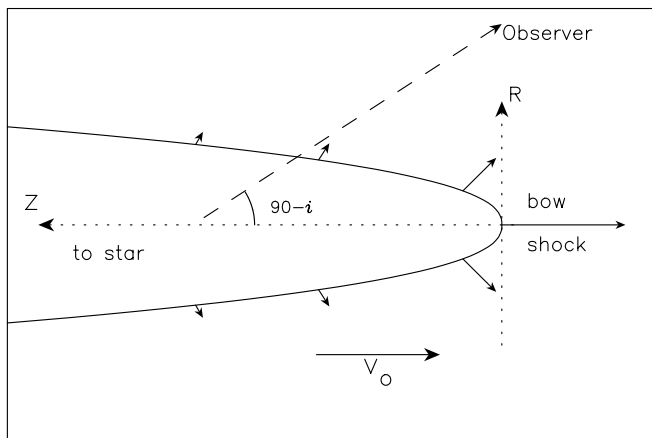


FIG. 19.—Schematic diagram of the jet-driven bow shock model in a cylindrical coordinate system. v_o is the bow shock velocity and i is the inclination of the model to the plane of the sky. The z -axis is along the center of the bow shock with $z = 0$ at the tip and positive z points to the star. The vectors indicate the velocities of the material in the shell.

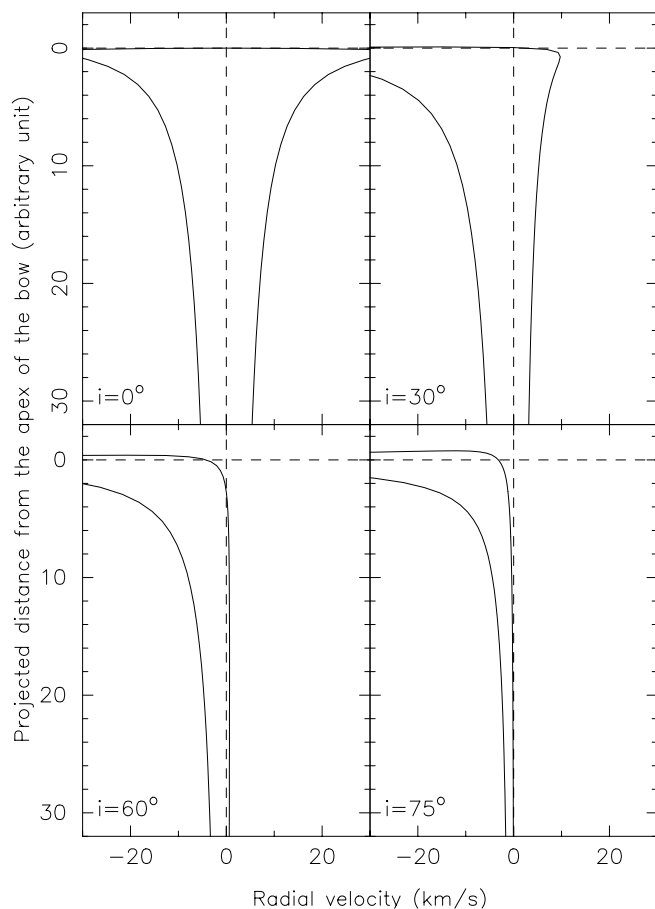


FIG. 20.—PV diagrams for the jet-driven bow shock model at four different inclinations to the plane of the sky. The diagrams were calculated using the algorithm in the appendix of Smith et al. (1997). The bow shock velocity is assumed to be 100 km s^{-1} . The zero point on the y -axis is the bow shock tip.

Comparing with the PV diagrams in the jet-driven bow shock model, we see that a model at an inclination of $i \sim 5^\circ$ can qualitatively account for the spur structures in the PV diagram of the HH 212 outflow, especially toward the bow shocks SB3 and NB3, consistent with earlier work (Claussen et al. 1998). The reflection symmetry of the PV structures at SB3 and NB3 is a consequence of the inclination angle of the jet. The PV structure of the bow shock SB4 is weaker and one sided, and could have a slightly different inclination angle. The dual bow shock structure SB3 and SB4 may be indicative of internal variations in the jet. If the jet velocity varies, the higher velocity material can drive an internal bow shock in the jet (Raga 1993; Suttner et al. 1997). The bow shock expands and eventually interacts with the existing shell. In this picture, the CO emission associated with bow shock SB3 arises from an expanded internal bow shock, while the CO emission associated with SB4 arises from an earlier interaction of the jet with ambient material.

4.1.2. A Wind-driven-Shell Model for VLA 05487

In the northern lobe of VLA 05487, the CO emission forms a parabolic structure surrounding the H_2 jet. The PV structure along the jet axis is also parabolic. These features can not be matched to a jet-driven bow shock model but can be naturally produced by the wide-angle-wind model of Shu et al. (2000).

In the wide-angle-wind model, a young star blows a radial wind into the ambient material, driving a forward shock, which runs ahead of the wind bubble, sweeping up the ambient material and producing the molecular outflow (Shu et al. 2000). The wind could be stratified in density by emerging from an extended disk (see Ostriker 1997) or by the action of latitudinal magnetic stresses in a rotating protostellar wind (Shu et al. 1995). The density and velocity structure of the outflow depend on the wind stratification and on the structure of the ambient core. For a radially-blowing force-free magnetized wind with thrust $\propto 1/\sin^2\theta$ propagating into a flattened ambient core with density $\propto \sin^2\theta/r^2$, the swept-up shell is a radially expanding parabola with a Hubble law velocity structure (see Fig. 5a in Li & Shu 1996), producing a parabolic PV structure at any inclination.

Figure 21 shows a schematic diagram of the model in a cylindrical coordinate system. In this coordinate system, the structure and velocity of the shell can be written as follows:

$$z = CR^2 \quad v_R = v_0 Rv_z = v_0 z, \quad (1)$$

where C and v_0 are free parameters. The PV diagrams along the major axis for the model at four different inclinations to the plane of the sky are shown in Figure 22 for $C = 0.30 \text{ arcsec}^{-1}$ and $v_0 = 0.33 \text{ km s}^{-1} \text{ arcsec}^{-1}$. To calculate the channel maps for comparison with the observations, the shell is assumed to have a thickness of a few arcsecs. The velocity is centered at the middle of the shell and drops exponentially to half at the edges of the shell. In addition, the CO emissivity is assumed to fall off as $1/(1 + (z/z_0)^2)$, with z_0 representing the cloud core.

The best-fit parameters for the VLA 05487 outflow are $C = 0.22 \pm 0.05 \text{ arcsec}^{-1}$ and $v_0 = 0.32 \pm 0.05 \text{ km s}^{-1} \text{ arcsec}^{-1}$ with $i = 19^\circ \pm 3^\circ$. These three parameters are determined by three different properties of the outflow. C is determined by the spatial emission structure of the outflow. Once C is known, v_0 and i are determined by the tilt and

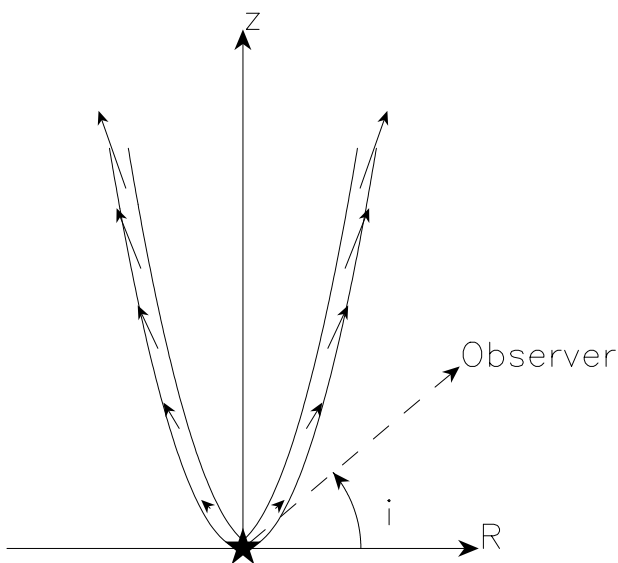


FIG. 21.—Schematic diagram of the wind-driven-shell model in a cylindrical coordinate system. i is the inclination of the model to the plane of the sky. The z -axis is defined to be along the symmetry axis of the wind with $z = 0$ at the location of the driving source. The vectors indicate the velocities of the material in the shell.

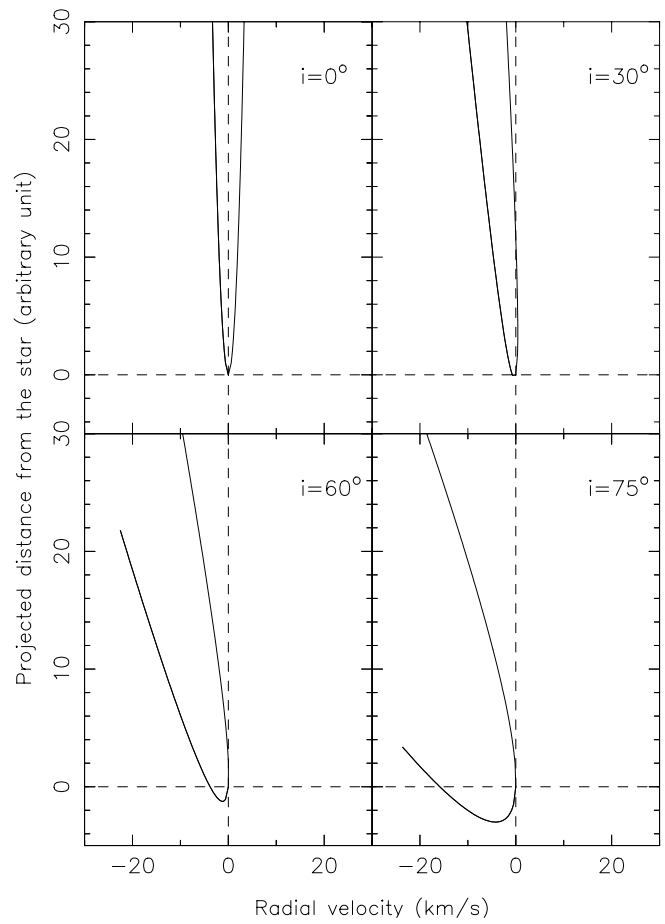


FIG. 22.—PV diagrams for the wind-driven-shell model at four different inclinations to the plane of the sky. The diagrams are calculated using the model from Li & Shu (1996) with $C = 0.30 \text{ arcsec}^{-1}$ and $v_0 = 0.33 \text{ km s}^{-1} \text{ arcsec}^{-1}$.

opening angle of the PV structure. The comparisons of the PV diagram, integrated emission, and channel maps are presented in Figures 23 and 24. As can be seen from the figures, the model is a good fit to the observations. Since the emissivity falls off with distance, the emission structure at high velocity is only seen at the end near the source, so the observations show an open structure. As the velocities increase to the red, the emission structure changes from a closed structure to an open structure, and moves away from the source, consistent with the observations. Within the wind model, the dynamical age of the outflow is given by $1/v_0$. Thus, the dynamical age of the VLA 05487 outflow is about 7000 years.

It is unclear at this point if the inclination of 19° is consistent with other aspects of the system. Based on the H_2 emission, the radial velocity of the northern jet of VLA 05487 (IRS 2) was found to be $180 \pm 50 \text{ km s}^{-1}$ (Garnavich et al. 1997). At our estimated inclination of $19^\circ \pm 3^\circ$, the real jet velocity would be between 350 and 830 km s^{-1} . The plausible H_2 jet velocity for low-mass young stars ranges from 100 up to 500 km s^{-1} (Coppin et al. 1998; Micono et al. 1998), so VLA 05487 may have a fast jet. Alternatively, the H_2 jet is a small scale structure close to the source, while the CO outflow is a large scale structure representing the cumulative effect of the interactions. It is possible that the small H_2 jet is at higher inclination than the average incli-

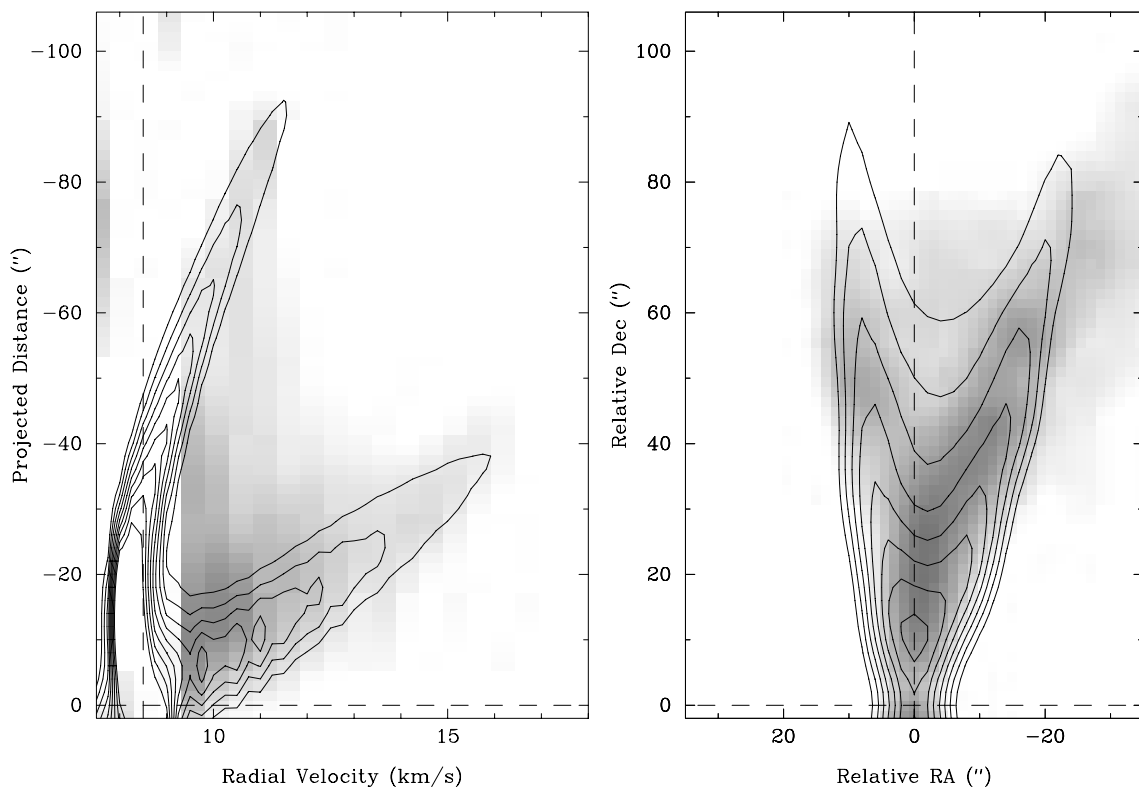


FIG. 23.—Comparison between the wind-driven model and the observations for the northern lobe of the VLA 05487 outflow. The gray-scale images are the observations, the contours are calculated from the wind-driven model. The left panel shows the comparison of the PV diagram cut along the jet axis. The right panel shows the comparison of the integrated emission.

nation of the large scale CO outflow, so the corresponding real jet velocity could be smaller. Further observations are needed to resolve this possible discrepancy.

4.1.3. A Candidate for a Jet-driven Bow Shock System: HH 240/241

In the HH 240/241 flow, the CO emission in the western lobe curves around the H_2 bow shock structure HH 240A, suggesting that the CO emission arises in material interacting with the bow shock (Fig. 3). The PV structure for this lobe clearly indicates that there is a broad range of velocities near the bow tip with the velocity increasing toward the bow tip (Fig. 8). Comparing the PV structure to that of the jet-driven bow shock model (Fig. 20), it seems that the PV structure can be described fairly well with a model at an inclination of 30° to 60° . In the eastern lobe, the CO emission shows a shell structure excavated around the H_2 bow shocks. However, the PV structure for this lobe is not simple to interpret in the context of either model.

The kinematics of the outflows can be further investigated using PV diagrams cut across the jet axis at different projected distances from the source. Figure 25 shows these PV diagrams for the western lobe of HH 240/241. The projected distance from the source is indicated at the upper right corner in each panel. The PV diagrams show asymmetric structures with the average velocity becoming increasingly blueshifted with increasing projected distance. Notice that the emission is weak to the north as seen in Figure 3. The asymmetric structures extend toward higher blueshifted velocity, with the highest blueshifted velocities at larger projected distance from the source but close to the outflow axis.

Figure 26 shows PV diagrams cut across the major axis for the jet-driven bow shock model and the wind-driven-shell model at inclinations of 10° and 45° . For the jet model, the distance is with respect to the bow apex, while for the wind model, the distance is to the driving source. At low inclination, both models predict an elliptical structure for the PV diagram. At high inclination, the PV structure for the wind model is still an elliptical structure; however, the PV structure for the jet model becomes an asymmetric structure pointing toward higher velocities. This asymmetry is due to the broader range of velocities near the bow shock tip; the lower velocity bow wings also have lower velocity dispersion. The structures in the HH 240/241 flow are qualitatively similar to the jet model, but the observed flow lacks emission on the north side of the flow axis, perhaps owing to an asymmetry in the cloud or a change of jet direction.

4.1.4. What drives the HH 111 Molecular Outflow ?

From the PV diagram along the jet axis (Fig. 9), it is clear that there are two different PV structures in the HH 111 outflow: a parabolic PV structure extending out to bow shocks E/F and a spur PV structure extending to bow shock P. Figure 27 shows the PV diagrams cut across the jet axis at different projected distances. The upper six panels trace the inner component; the lower six panels trace the outer component. For the inner component, the PV diagrams across the jet axis show mainly symmetric structures. Thus, the parabolic inner PV structure seems to indicate a wide-angle-wind interaction. This PV structure was fitted by Nagar et al. (1997) with a radially expanding parabolic shell within the context of the wind-driven-shell model. However, the emission associated with this PV structure

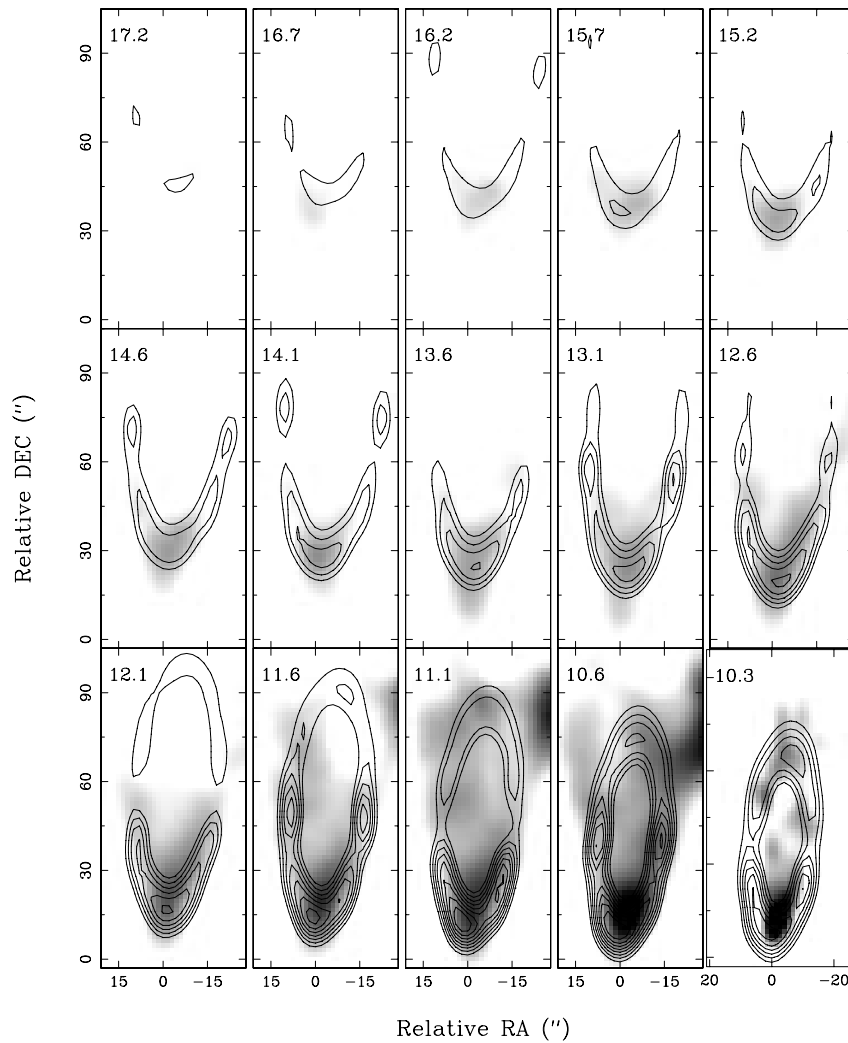


FIG. 24.—Comparison of the channel maps with the wind-driven model calculation for the VLA 05487 outflow. The gray-scale images are the observations, the contours are the calculations.

ends near bow shocks E/F, about where the cloud core ends (see Fig. 4). For the outer component, the PV diagrams across the jet axis show asymmetric structures similar to that seen in the PV diagrams of the jet model at large inclination (see Fig. 26). Therefore, the outer spur structure seems to suggest the presence of a bow shock interaction. However, the inclination of the outflow would have to be more than 30° to account for the lack of redshifted and

low-velocity blueshifted emission. This inclination is very different from that obtained from measurements of the radial velocity and proper motions of the jet, only about 10° (Reipurth et al. 1992).

No single model can provide a consistent explanation for the emission structure and kinematics of the HH 111 flow, so perhaps a combined model is required (Cabrit et al. 1997). On the other hand, the two kinematic and emission

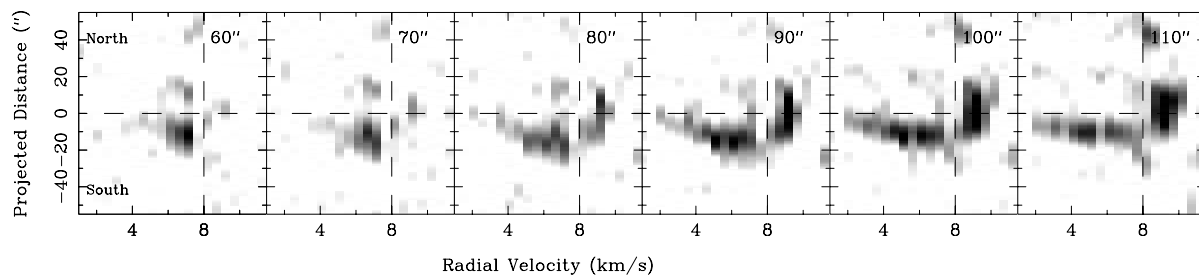


FIG. 25.—PV diagrams cut across the jet axis for the western lobe of the HH 240/241 outflow at different distances from the source. The distances from the source are indicated at the upper right corner of each panel.

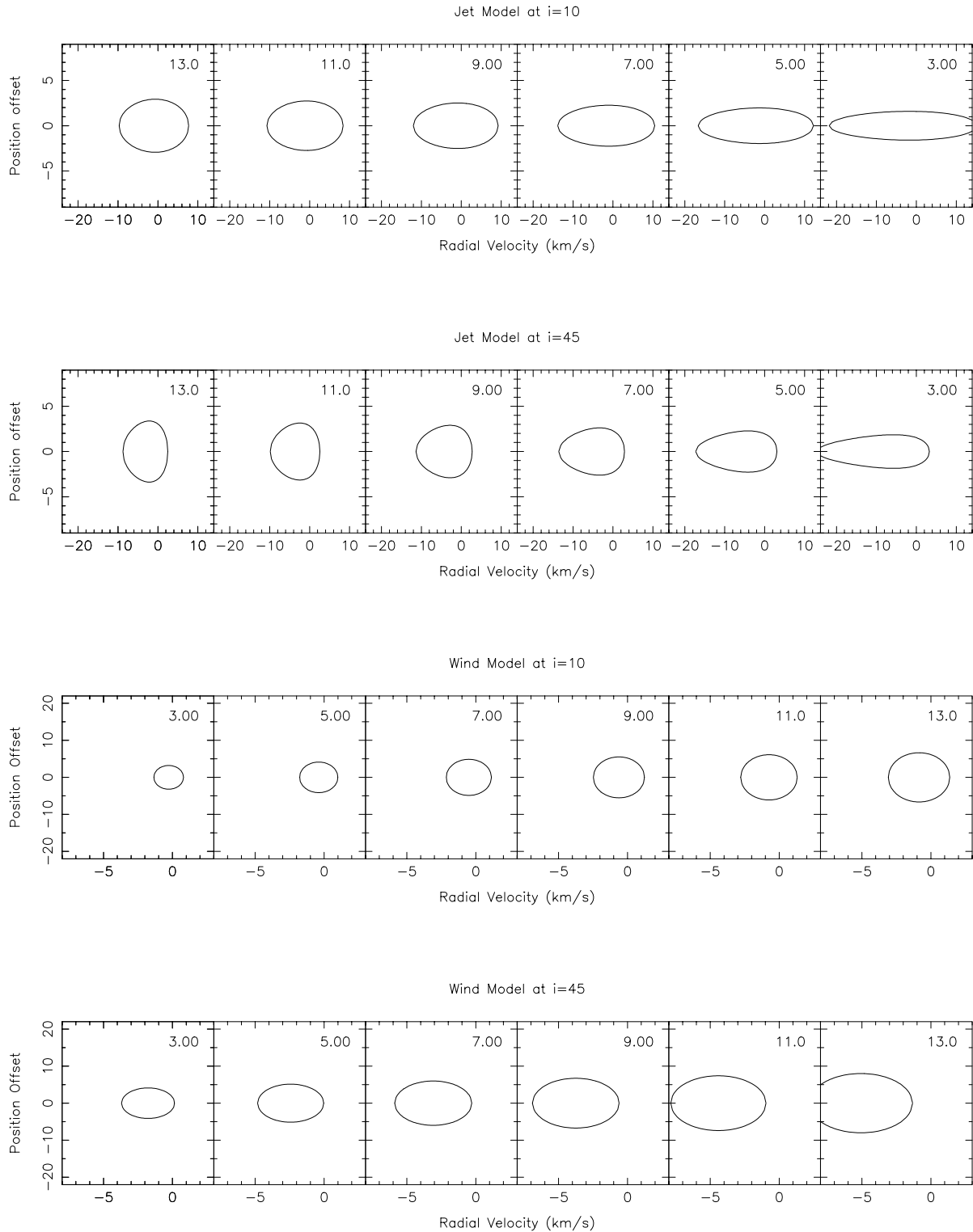


FIG. 26.—PV diagrams cut across the jet axis for the jet-driven bow shock model and wind-driven-shell model at inclinations of 10° and 45° to the plane of the sky. For the jet model, the distance is with respect to the bow apex, while for the wind model, the distance is with respect to the driving source.

structures could be a consequence of major time variability of the underlying jet/wind. In the infrared and optical observations, a series of knots and bow shocks are seen in the jet (Gredel & Reipurth 1994; Coppin et al. 1998; Reipurth et al. 1999). These knots and bow shocks can be produced if the velocity of the underlying jet/wind changes (Raga 1993; Suttner et al. 1997). In this picture, the inner emission struc-

ture of HH 111 arises from the combined effect of many bow shock interactions, while the outer emission structure is more pristine (see HH 212 for a possible analogy). Alternatively, since bow shocks E/F are near the cloud edge, the different PV structures may result from the interaction of the underlying jet/wind with the different ambient environment. Or the material detected beyond bow shocks E/F

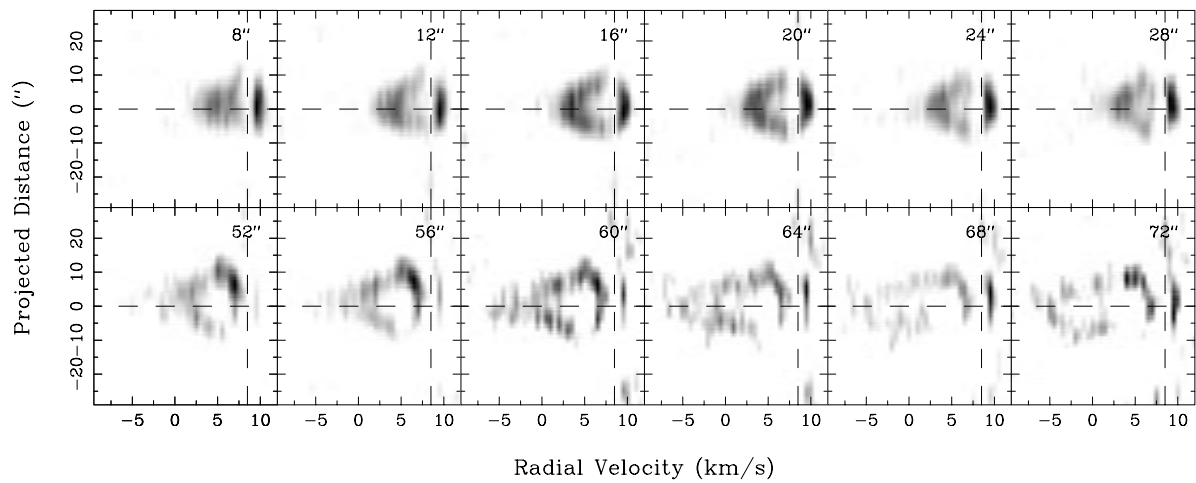


FIG. 27.—PV diagrams cut across the jet axis for the western lobe of the HH 111 outflow. Upper six panels show the inner emission structure, and lower six panels show the outer emission structure, where the division between inner and outer is bow shocks E/F. The distances from the source are indicated at the upper right corner of each panel.

may be the material dragged along from inside the cloud as suggested by Cernicharo & Reipurth (1996). Further study of the dynamics is needed to explore these possibilities.

4.1.5. What drives the RNO 91 Outflow ?

For RNO 91, the CO emission forms a U-shaped structure around the major axis. This outflow has been modeled with an expanding shell to quantitatively explain PV diagrams cut across the jet axis by Bence et al. (1998). The PV structure in Figure 10 is not clear due to the lack of emission at high velocity and contamination of the emission at low velocity. In the PV diagram, if we consider the arm extending at the source position and the arm extending at about $400''$ to the south of the driving source as the two sides of a parabola, then the RNO 91 outflow may be driven by a wide-angle wind.

The best-fit parameters for the RNO 91 outflow are $C = 0.02 \pm 0.004 \text{ arcsec}^{-1}$ and $v_o = 0.038 \pm 0.01 \text{ km s}^{-1} \text{ arcsec}^{-1}$ with $i = 20^\circ \pm 4^\circ$. Figures 28 and 29 presents comparisons between the model and observations. Similar to the VLA 05487 flow, the CO emission structure changes from a closed lobe structure to an opened structure as the velocity increases to the blue. However, it is difficult to match the channel maps since the outflow is not symmetric about the driving source and the outflow axis changes with distance. The axis initially is more north-south oriented, and it gradually curves eastward with increasing distance. For simplicity, we used one parabola centered on the driving source with a mean outflow axis. As can be seen, this simple model reproduces the essential features of the observations, but with the peak position shifting a little to the east at high velocity owing to the symmetry of the model

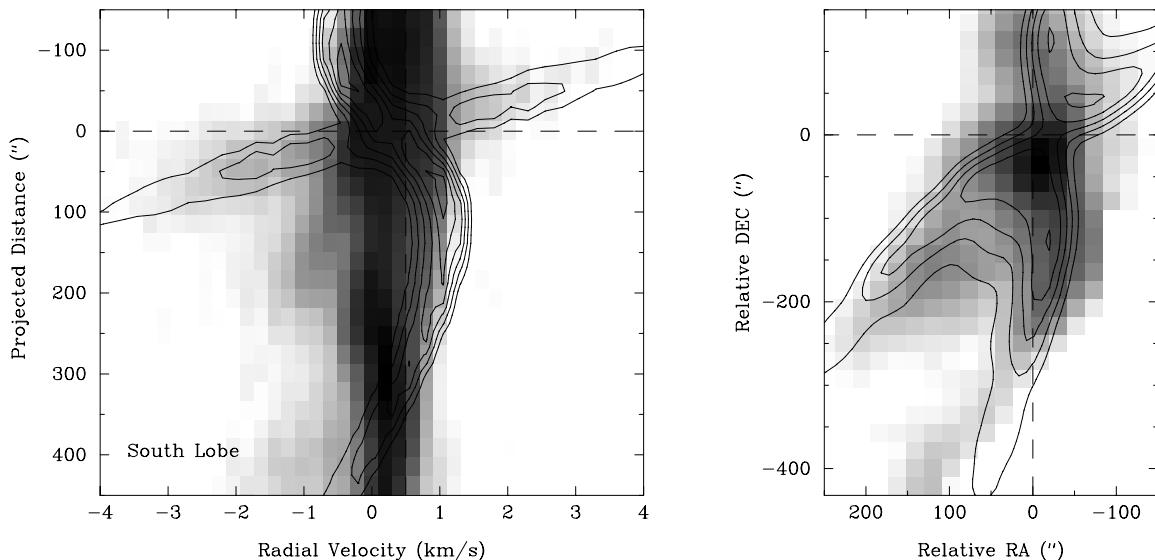


FIG. 28.—Comparison between the wind-driven model and the observations for the RNO 91 outflow. The gray-scale images are the observations, the contours are calculated from the wind-driven model. The left panel shows the comparison of the PV diagram cut along the major axis. The right panel shows the comparison of the integrated emission.

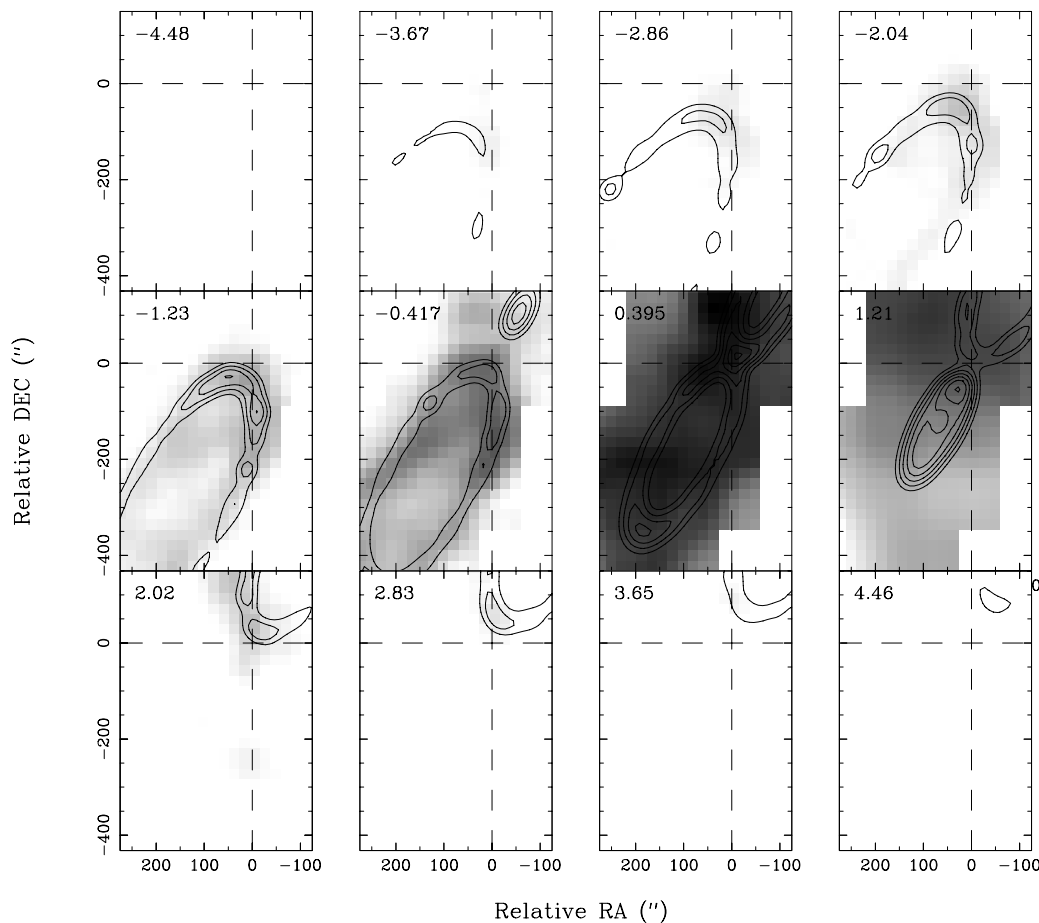


FIG. 29.—Comparison of the channel maps with the model calculation for RNO 91. The gray-scale images are the observations, the contours are calculated from the wind-driven model.

about the driving source. The dynamical age of this outflow is estimated to be 20,000 years. The inclination is consistent with that derived for the disk by Weintraub et al. (1994). They estimated the inclination to be 20° – 30° based on modeling the scattered light.

4.2. Are Two Different Models Necessary?

Since the two types of kinematics appear together in some outflows, such as HH 111, it is natural to ask if a single model might be able to produce the different kinematics and thus explain all of the molecular outflows in our observations.

4.2.1. Could a Jet-driven Bow Shock Model be Universal?

The jet-driven bow shock model can qualitatively account for the velocity spur structure seen in the HH 212 and HH 240/241 outflows, as well as the morphological relation between the CO emission and H_2 emission. However, the jet-driven models generally have problems reproducing the widths seen in these outflows. Owing to strong cooling of the high-pressure shocked material that drives transverse motion, the predicted and simulated outflow lobe radii are always 3–5 times the jet radius (Masson & Chernin 1993; de Gouveia dal Pino & Benz 1993; Cabrit et al. 1997; Smith et al. 1997; Downes & Ray 1999). An extremely large jet, radius of $\sim 10^3$ AU, would be needed to reproduce the observed width in these outflows.

In addition, jet models suffer a generic difficulty in coupling the forward momentum of the jet into the molecular outflow (Lada & Fich 1996). It is argued that mixing of material at the shock front may mitigate this problem but detailed treatments have yet to prove this (Masson & Chernin 1993; Raga, Cabrit, & Canto 1995; Smith et al. 1997).

The VLA 05487 outflow has a parabolic PV structure (see Fig. 6). The kinematics of the RNO 91 outflow is less clear but seems similar to the VLA 05487 outflow. To reproduce these outflows, the jet model faces a larger problem in that it not only needs to reproduce the width but also the kinematics. The VLA 05487 outflow in our observations only represents the inner quarter of the whole outflow which extends $8'$ to the north (Reipurth & Olberg 1991). The RNO 91 outflow is an old outflow being driven by a class II/III source. Therefore, it is possible that these two CO outflows are the cumulative result of a series of oblique shocks produced by a series of ejections. The HH 111 outflow provides its own challenge for the jet model in that producing the spur PV structure (see Fig. 9) with a bow shock would require a significantly larger inclination angle than that of the optical/ H_2 jet.

Overall, a simple steady jet model has difficulty producing the width, the parabolic PV structure, as well as the motion along the jet axis. It has been argued that additional mechanisms, such as interactions with moving ambient

material, jet wandering, and jet spraying, can increase the forward motion, as well as the opening angle, of the outflows (Cabrit et al. 1997). Our data provide some evidence for changes in jet direction in that the shock interaction features are not collinear, although these nonlinearities could also be due to an instability in the jet. Further studies are needed to determine if more sophisticated jet models can match the observations in detail.

4.2.2. *Could a Wind-driven-Shell Model be Universal?*

The wind model quite naturally produces cavities with parabolic shapes and parabolic PV structures. The key issue for the wind model is whether it can also cause localized bow shock features with spur PV structures. The magnetized radial wind model of Shu et al. (1995) has a density-enhanced region on the axis that gives the appearance of a highly collimated jet (Shang et al. 1998). If this "jet" can produce discrete bow shock features, the wind model may be able to reproduce the HH 212, HH 111, and HH 204/241 outflows. The Shu et al. wind model has a time-independent wind, so it cannot produce internal shocks, but velocity variability in the wind would undoubtedly create internal shocks and splashing. We will explore this type of model in a future publication.

Alternatively, it is possible that different models are required for outflows at different evolutionary stages. It has been proposed that the opening angle of the high-velocity stellar material increases with age, going from a highly collimated jet in very young objects to a very wide angle wind in old systems (Velusamy & Langer 1998; Richer et al. 2000). VLA 05487, HH 212 and HH 240/241 are class 0/I sources, HH 111 is a class I source, while RNO 91 is a class II/III source. Our survey sample is too small to provide a persuasive conclusion about the evolution of the driving mechanism.

5. CONCLUSION

High spatial resolution CO observations toward five molecular outflow systems have revealed a variety of structures and kinematics in the molecular outflows. Our main conclusions are the following:

1. Low-density cavities created by the stellar wind/jet are present in outflows of different collimations and evolutionary stages. The CO emission forms rough shell structures around the cavities, with material at higher velocity occurring further out from the source along the flow axis.
2. There are striking morphological correspondences between the H₂ and CO emission in the HH 212 and HH

240/241 systems. The CO emission closely surrounds the outflow axis with the brightest CO emission cradling the prominent H₂ bow shocks on the downwind side.

3. Two distinctive kinematic features are evident in position-velocity (PV) diagrams cut along the outflow axis: a parabolic structure originating at the driving source as found for VLA 05487 and HH 111, and a convex spur structure with the high velocity tip near the H₂ bow shock structure best seen in HH 212 and HH 240/241.

4. The CO outflows of HH 212 and HH 240/241 are best explained by a jet-driven bow shock model. The jet-driven bow shock model not only produces the morphological coincidence between the H₂ and CO emission, but also produces a broad range of velocities near the H₂ bow shock structures and qualitatively explains the spur PV structures in these sources.

5. The CO outflows driven by VLA 05487 and RNO 91, which both lack H₂ shock features, are reasonably described with a radially expanding parabolic shell, consistent with the wind-driven-shell model. The model not only reproduces the parabolic emission structures, but also the parabolic PV structures in these sources.

6. The HH 111 outflow has a complicated kinematics with both parabolic and spur PV structures. A combination of a jet-driven bow shock model and a wind-driven-shell model may be required to produce the HH 111 outflow. It is also possible that the cloud edge may play a critical role in generating the kinematics in the outer portion of the outflow.

Additional detailed numerical modeling of the jet and wind models are needed to understand if the cumulative effect of time variable jets can create more open outflow structures, or if there are realistic conditions under which wide-angle winds can create localized bow shock structures and their characteristic kinematics.

We thank Stephen White for providing part of the HH 212 BIMA data and Neil Nagar for providing part of the HH 111 BIMA data. We thank Christopher Davis for providing the H₂ images of HH 111 and HH 240/241, Mark McCaughrean for HH 212, and Peter Garnavich for VLA 05487. We thank the FCRAO for granting observing time and Mark Heyer for supporting the observations. We thank Rick Forster and the BIMA staff for their efforts in running and maintaining the array. This work was supported in part by NSF AST-13716 and NASA NAG-54429.

REFERENCES

- André, P., & Montmerle, T. 1994, *ApJ*, 420, 837
 Bachiller, R. 1996, *ARA&A*, 34, 111
 Bachiller, R., Guilloteau, S., Dutrey, A., Planesas, P., & Martin-Pintado, J. 1995, *A&A*, 299, 857
 Bally, J., & Lada, C. J. 1983, *ApJ*, 265, 824
 Bence, S. J., Padman, R., Isaak, K. G., Wiedner, M. C., & Wright, G. S. 1998, *MNRAS*, 299, 965
 Bence, S. J., Richer, J. S., & Padman, R. 1996, *MNRAS*, 279, 866
 Bohigas, J., Persi, P., & Tapia, M. 1993, *A&A*, 267, 168
 Cabrit, S., Raga, A., & Gueth, F. 1997, in *IAU Symp.*, 182, Herbig-Haro Flows and the Birth of Stars, ed. B. Reipurth & C. Bertout (Dordrecht: Kluwer), 163
 Chernin, L.M., Masson, C.R., Gouveia dal Pino, E.M., & Benz, W. 1994, *ApJ*, 426, 204
 Cernicharo, J., & Reipurth, B. 1996, *ApJ*, 460, L57
 Claussen, M. J., Marvel, K. B., Wootten, A., & Wilking, B. A. 1998, *ApJ*, 507, L79
 Cohen, M. 1980, *AJ*, 85, 29
 Coppin, K. E. K., Davis, C. J., & Micono, M. 1998, *MNRAS*, 301, L10
 Davis, C. J., Mundt, R., & Eisloffel, J. 1994, *ApJ*, 437, L55
 Davis, C. J., Ray, T. P., Eisloffel, J., & Corcoran, D. 1997, *A&A*, 324, 263
 de Gouveia dal Pino, E. M., & Benz, W. 1993, *ApJ*, 410, 686
 Downes, T. P., & Ray, T. P. 1999, *A&A*, 345, 977
 Fukui, Y., Iwata, T., Mizuno, A., Bally, J., & Lane, A. P. 1993, *Protostars and Planets III*, ed. E. H. Levy & J. I. Lunine (Tucson: Univ. Arizona Press), 603
 Garnavich, P. M., Noriega-Crespo, A., Raga, A. C., & Bohm, K.-H. 1997, *ApJ*, 490, 752
 Gredel, R., & Reipurth, B. 1994, *A&A*, 289, L19
 Gueth, F., & Guilloteau, S. 1999, *A&A*, 343, 571
 Gueth, F., Guilloteau, S., & Bachiller, R. 1996, *A&A*, 307, 891
 Hodapp, K.-W. 1994, *ApJS*, 94, 615
 Hodapp, K.-W., & Ladd, E. F. 1995, *ApJ*, 453, 715
 Kumar, M. S. N., Anandarao, B. G., & Davis, C. J. 1999, *A&A*, 344, L9
 Lada, C. J. 1985, *ARA&A*, 23, 267
 Lada, C. J., & Fich, M. 1996, *ApJ*, 459, 638

- Levreault, R. M. 1988, *ApJ*, 330, 897
- Li, Z.-Y., & Shu, F. H. 1996, *ApJ*, 472, 211
- Masson, C. R., & Chernin, L. M. 1993, *ApJ*, 414, 230
- Mathieu, R. D., Myers, P. C., Schild, R. E., Benson, P. J., & Fuller, G. A. 1988, *ApJ*, 330, 385
- Matzner, C. D., & McKee, C. F. 1999, *ApJ*, 526, L109
- McKee, C. F., Hollenbach, D. J., Seab, G. C., & Tielens, A. G. G. M. 1987, *ApJ*, 318, 674
- Meyers-Rice, B. A., & Lada, C. J. 1991, *ApJ*, 368, 445
- Myers, P. C., Heyer, M., Snell, R. L. & Goldsmith, P. F. 1988, *ApJ*, 324, 907
- Micono, M., Davis, C. J., Ray, T. P., Eisloffel, J., & Shetrone, M. D. 1998, *ApJ*, 494, L227
- Nagar, N. M., Vogel, S. N., Stone, J. M., & Ostriker, E. C. 1997, *ApJ*, 482, L195
- Ostriker, E. C. 1997, *ApJ*, 486, 291
- Raga, A. C. 1993, *Ap&SS*, 208, 163
- Raga, A., & Cabrit, S. 1993, *A&A*, 278, 267
- Raga, A. C., Cabrit, S., & Canto, J. 1995, *MNRAS*, 273, 422
- Reipurth, B., Bally, J., & Devine, D. 1997a, *AJ*, 114, 2708
- Reipurth, B., & Cernicharo, J. 1995, *Rev. Mexicana Astron. Astrofis. Conf. Ser.* 1, 43
- Reipurth, B., Chini, R., Krugel, E., Kreysa, E., & Sievers, A. 1993, *A&A*, 273, 221
- Reipurth, B., Hartigan, P., Heathcote, S., Morse, J. A., & Bally, J. 1997b, *AJ*, 114, 757
- Reipurth, B., & Olberg, M. 1991, *A&A*, 246, 535
- Reipurth, B., Raga, A. C., & Heathcote, S. 1992, *ApJ*, 392, 145
- Reipurth, B., Yu, K., Rodriguez, L. F., Heathcote, S., & Bally, J. 1999, *A&A*, 352, L83
- Richer, J. Shepherd, D., Cabrit, S., Bachiller, R., & Churchwell, E. 2000, in *Protostars and Planets IV*, ed. V. Mannings, A. P. Boss & S. S. Russell (Tucson: Univ. Arizona Press), 867
- Rodriguez, L. F., & Reipurth, B. 1994, *A&A*, 281, 882
- Rodriguez, L. F., Reipurth, B., Raga, A. C., & Canto, J. 1998, *Rev. Mexicana Astron. Astrofis.*, 34, 69
- Shang, H., Shu, F. H., & Glassgold, A. E. 1998, *ApJ*, 493, L91
- Shu, F. H., Ruden, S. P., Lada, C. J., & Lizano, S. 1991, *ApJ*, 370, L31
- Shu, F. H., Najita, J., Ostriker, E. C., & Shang, H. 1995, *ApJ*, 455, L155
- Shu, F. H., Najita, J., Shang, H., & Li, Z.-Y. 2000, in *Protostars and Planets IV*, ed. V. Mannings, A. P. Boss & S. S. Russell (Tucson: University of Arizona Press), 789
- Smith, M. D., Suttner, G., & Yorke, H. W. 1997, *A&A*, 323, 223
- Stone, J. M., & Norman, M. L. 1994, *ApJ*, 420, 237
- Suttner, G., Smith, M. D., Yorke, H. W., & Zinnecker, H. 1997, *A&A*, 318, 595
- Terebey, S., Chandler, C. J., & Andre, P. 1993, *ApJ*, 414, 759
- Velusamy, T., & Langer, W. D. 1998, *Nature*, 392, 685
- Völker, R., Smith, M. D., Suttner, G., & Yorke, H. W. 1999, *A&A*, 343, 953
- Weintraub, D. A., Tegler, S. C., Kastner, J. H., & Rettig, T. 1994, *ApJ*, 423, 674
- Wiseman, J. J., Wooten, A., Fuller, G. A., Zinnecker, H., & McCaughrean, M. J. 1999, *A&AS*, 195, 0201
- Wouterloot, J. G. A., & Walmsley, C. M. 1986, *A&A*, 168, 237
- Wu, Y., Huang, M., & He, J. 1996, *A&AS*, 115, 283
- Yang, J., Ohashi, N., Yan, J., Liu, C., Kaifu, N., & Kimura, H. 1997, *ApJ*, 475, 683
- Zinnecker, H., Bastien, P., Arcoragi, J.-P., & Yorke, H. W. 1992, *A&A*, 265, 726
- Zinnecker, H., McCaughrean, M. J., & Rayner, J. T. 1998, *Nature*, 394, 862

ERRATUM

In the paper “CO Outflows from Young Stars: Confronting the Jet and Wind Models” by C.-F. Lee, L. G. Mundy, B. Reipurth, E. C. Ostriker, and J. M. Stone (ApJ, 542, 925 [2000]), Figure 2 did not show the correct H₂ image and should be replaced by the one presented here. In addition, equation (1) did not have the correct format and should be written as follows:

$$z = CR^2, \quad v_R = v_0 R, \quad v_z = v_0 z. \quad (1)$$

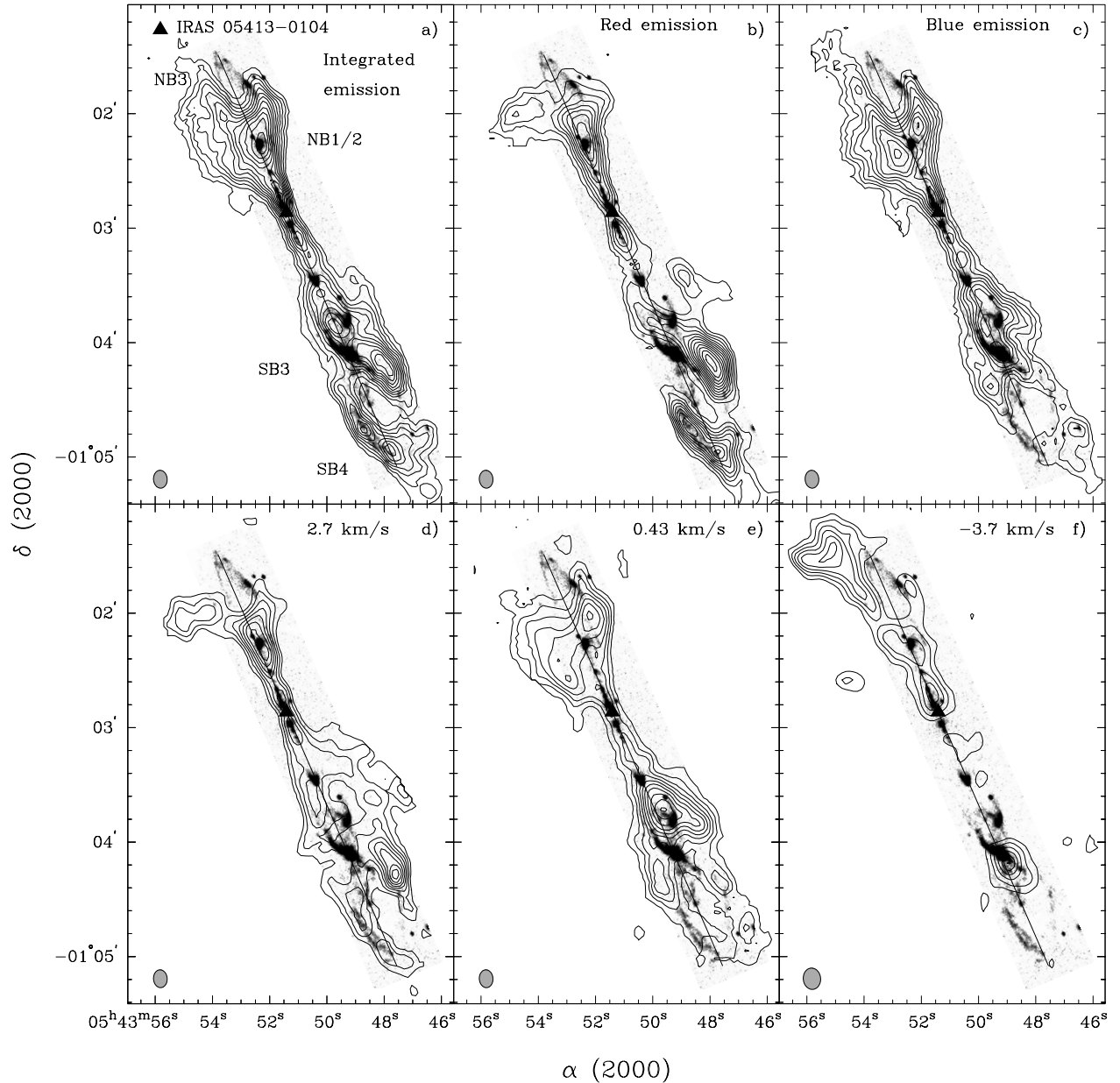


FIG. 2.—CO outflow emission of HH 212 in the BIMA observations overlaid on a gray-scale H₂ image provided by Zinnecker et al. (1998). The line indicates the direction of the H₂ jet centered at IRAS 05413–0104. The labels, NB3, NB1/2, SB3, and SB4, denote the locations of H₂ bow shocks as enumerated by Zinnecker et al. (1998). (a) The CO emission integrated from -4.2 to 5.5 km s^{-1} . This velocity range includes both the red and blue outflow emission. (b) The red emission integrated from 1.96 to 5.51 km s^{-1} . (c) The blue emission integrated from -4.5 to 1.7 km s^{-1} . (d) and (e) Channel maps at two redshifted velocities. (f) The emission at -3.7 km s^{-1} averaged over 3 km s^{-1} velocity interval to improve the signal-to-noise ratio. The contours in (a) start at $2 \text{ Jy beam}^{-1} \text{ km s}^{-1}$ with a step size of $2 \text{ Jy beam}^{-1} \text{ km s}^{-1}$. The contours in (b) and (c) start at $1.5 \text{ Jy beam}^{-1} \text{ km s}^{-1}$ with a step size of $1.5 \text{ Jy beam}^{-1} \text{ km s}^{-1}$. For (d) and (e), the contours start at 2.5 Jy beam^{-1} with a step size of 1 Jy beam^{-1} . For (f), the contours start at 0.6 Jy beam^{-1} with a step size of 0.3 Jy beam^{-1} . The beam size is $9''.4 \times 7''.2$.